

A Model Independent Analysis of Higgs-boson pair production at the LHC

Chih-Ting Lu¹, Jung Chang¹, Kingman Cheung^{1,2,3}, and Jae Sik Lee^{3,4}

¹ *Department of Physics, National Tsing Hua University, Hsinchu 300, Taiwan*

² *Division of Quantum Phases and Devices, School of Physics,
Konkuk University, Seoul 143-701, Republic of Korea*

³ *Physics Division, National Center for Theoretical Sciences, Hsinchu, Taiwan*

⁴ *Department of Physics, Chonnam National University,
300 Yongbong-dong, Buk-gu, Gwangju, 500-757, Republic of Korea*

(Dated: July 29, 2022)

Abstract

Higgs-boson pair production is well known being capable to probe the trilinear self-coupling of the Higgs boson, which is one of the important ingredients of the Higgs sector itself. Pair production then depends on the top-quark Yukawa coupling $g_t^{S,P}$, Higgs trilinear coupling λ_{3H} , and a possible dim-5 contact-type $ttHH$ coupling $g_{tt}^{S,P}$, which may appear in some higher representations of the Higgs sector. We take into account the possibility that the top-Yukawa and the $ttHH$ couplings involved can be CP violating. We calculate the cross sections and the interference terms as coefficients of the square or the 4th power of each coupling $(g_t^{S,P}, \lambda_{3H}, g_{tt}^{S,P})$ at various stages of cuts, such that the desired cross section under various cuts can be obtained by simply inputting the couplings. We employ the $HH \rightarrow \gamma\gamma b\bar{b}$ decay mode of the Higgs-boson pair to investigate the possibility of disentangle the triangle diagram from the box digram so as to have a clean probe of the trilinear coupling at the LHC. We found that the angular separation between the b and \bar{b} and that between the two photons is useful. We obtain the sensitivity reach of each pair of couplings at the 14 TeV LHC and the future 100 TeV pp machine. Finally, we also comment on using the $b\bar{b}\tau^+\tau^-$ decay mode in Appendix.

I. INTRODUCTION

A boson was discovered at the Large Hadron Collider (LHC) [1, 2]. After almost all the Run I data were analyzed, the measured properties of the new particle are best described by the standard-model (SM) Higgs boson [3, 4], which was proposed in 1960s [5]. The most constrained is the gauge-Higgs coupling $C_v \equiv g_{HWW} = 0.94_{-0.12}^{+0.11}$, which is very close to the SM value. On the other hand, the relevant top- and bottom-Yukawa couplings are not determined as precisely as C_v by the current data. Nevertheless, they are within 30 – 40% of the SM values.

Until now there is no information at all about the self-couplings of the Higgs boson, which emerges from the inner dynamics of the Higgs sector. For example, the trilinear couplings from the SM, two-Higgs doublet models (2HDM), and MSSM are very different from one another. Thus, investigations of the trilinear coupling will shed lights on the dynamics of the Higgs sector. One of the best probes is Higgs-boson-pair production at the LHC. There have been a large number of works of Higgs-pair production in the SM [6–8], in model-independent fashion [9, 10], and in special models beyond the SM [11] and in SUSY [12]. In the SM, Higgs-pair production receives contributions from two entangled sources, the triangle and box diagrams. The triangle diagram involves the Higgs self-trilinear coupling and the top-Yukawa coupling while the box diagram involves only the top-Yukawa coupling. In order to probe the effects of the Higgs trilinear coupling, we have to disentangle the triangle diagram from the box diagram. We anticipate that the triangle diagram, which contains an s -channel Higgs propagator, does not increase as much as the box diagram as the center-of-mass energy $\sqrt{\hat{s}} \equiv M_{HH}$ increases. Therefore, the box diagram tends to give more energetic Higgs-boson pairs than the triangle diagram. Thus, the opening angle in the decay products of each Higgs boson can be used to isolate the triangle-diagram contribution. Indeed, we found that the angular separation $\Delta R_{\gamma\gamma}$ and ΔR_{bb} between the decay products of the Higgs-boson pair are very useful variables to disentangle the two sources.

In some composite Higgs models, there exists the possibility of a dim-5 anomalous $ttHH$ contact coupling, which also contributes to Higgs-pair production via a triangle diagram. This triangle diagram is similar to the triangle diagram with the trilinear Higgs self coupling, except that it does not have the s -channel Higgs propagator. We shall show that the new contact diagram will give terms that can be combined with the terms of the triangle diagram,

as in Eq. (4). We note that the kinematic behavior of the triangle diagram induced by the dim-5 $ttHH$ contact interaction is different from that induced by the trilinear Higgs self coupling, because of the absence of the Higgs propagator in the contact diagram.

In this work, we adopt the model-independent approach, taking the liberty that the involved Higgs-boson couplings can be varied freely within reasonable ranges. The relevant couplings considered in this work are (i) the top-quark Yukawa coupling, (ii) the trilinear Higgs self-coupling, and (iii) the contact-type $ttHH$ coupling. In the top-quark Yukawa and contact-type $ttHH$ interactions, we take into account the possibility of the simultaneous presence of the scalar and pseudoscalar couplings which can signal CP violation.

Our strategy is first to find a useful expression for Higgs-boson pair production cross sections in terms of these couplings, see Eq. (7). The coefficient of each term depends on the collider energy \sqrt{s} , Higgs decay channels, experimental cuts, etc. Thus, such an expression enables us to easily obtain the cross section under various experimental conditions for arbitrary values of the couplings. Our aim is to extract the information on the Higgs couplings, especially on the Higgs self coupling by exploiting the expression. It is helpful to consider some experimental cuts which can isolate the contribution from the Higgs self coupling and lead to various cross sections with different dependence on the Higgs couplings. In this work, specifically, we employ the $b\bar{b}\gamma\gamma$ decay mode of the Higgs-boson pair and look into the angular separation between the b and \bar{b} and that between the photons. It is shown that one can map out the possible regions of Higgs couplings assuming certain values of measured cross sections.

In summary, the current work marks a number of improvements over previous published works as listed in the following:

1. We have included the CP-odd part in the top-Yukawa coupling. The CP-even and CP-odd parts are constrained by an elliptical-like equation by the current Higgs-boson data, as shown in Fig. 4 of Ref. [4].
2. We have included the dim-5 anomalous $ttHH$ contact coupling, as done in Ref. [10]. Furthermore, we also include the CP-odd part of this contact coupling.
3. We have calculated an easy-to-use expression to obtain the cross sections as a function of the involved couplings at each center-of-mass energy. We also obtain similar expressions in various kinematic regions such that one can easily obtain the cross sections

under the proposed experimental cuts for arbitrary values of the Higgs couplings.

4. With assumed uncertainties in the measurements of cross sections, we can map out the sensitivity regions of parameter space that can be probed at the LHC.

The organization of the work is as follows. In the next section, we describe the formalism for our model-independent approach and present an expression for the Higgs-boson pair production cross section in terms of various combinations of the Higgs couplings under consideration. In Section III, we examine the behavior of each term of the cross section versus energies. In Section IV, employing the $HH \rightarrow (\gamma\gamma)(b\bar{b})$ decay mode, we illustrate how to extract the information on the Higgs couplings by exploiting the angular separations between the Higgs decay products. There we also discuss the prospect for the 100 TeV pp machine. We conclude in Section V and offer a few comments with regard to our findings. In Appendix, we compare the SM cross sections at 14 TeV with those at 100 TeV for the process $pp \rightarrow H \rightarrow \gamma\gamma b\bar{b}$ and give some comments on the $\tau^+\tau^-b\bar{b}$ decay mode.

II. FORMALISM

Higgs-boson pair production via gluon fusion goes through a triangle diagram with a Higgs-boson propagator and also through a box diagram with colored particles running in it. The relevant couplings involved are top-Yukawa and the Higgs trilinear self coupling. We further explore the possibility of a dim-5 anomalous $ttHH$ contact coupling [10]. They are given in this Lagrangian:

$$-\mathcal{L} = \frac{1}{3!} \left(\frac{3M_H^2}{v} \right) \lambda_{3H} H^3 + \frac{m_t}{v} \bar{t} (g_t^S + i\gamma_5 g_t^P) t H + \frac{1}{2} \frac{m_t}{v^2} \bar{t} (g_{tt}^S + i\gamma_5 g_{tt}^P) t H^2. \quad (1)$$

In the SM, $\lambda_{3H} = g_t^S = 1$ and $g_t^P = 0$ and $g_{tt}^{S,P} = 0$. The differential cross section for the process $g(p_1)g(p_2) \rightarrow H(p_3)H(p_4)$ in the SM was obtained in Ref. [6] as

$$\frac{d\hat{\sigma}(gg \rightarrow HH)}{d\hat{t}} = \frac{G_F^2 \alpha_s^2}{512(2\pi)^3} \left[\left| \lambda_{3H} g_t^S D(\hat{s}) F_\Delta^S + (g_t^S)^2 F_\square^{SS} \right|^2 + \left| (g_t^S)^2 G_\square^{SS} \right|^2 \right] \quad (2)$$

where

$$D(\hat{s}) = \frac{3M_H^2}{\hat{s} - M_H^2 + iM_H\Gamma_H} \quad (3)$$

and $\hat{s} = (p_1 + p_2)^2$, $\hat{t} = (p_1 - p_3)^2$, and $\hat{u} = (p_2 - p_3)^2$ with $p_1 + p_2 = p_3 + p_4$. The loop functions $F_\Delta^S = F_\Delta$, $F_\square^{SS} = F_\square$, and $G_\square^{SS} = G_\square$ with $F_{\Delta,\square}$ and G_\square given in Appendix A.1 of Ref. [6].

Here we extend the result to including the CP-odd top-Yukawa and the anomalous $ttHH$ couplings:

$$\begin{aligned} \frac{d\hat{\sigma}(gg \rightarrow HH)}{d\hat{t}} &= \frac{G_F^2 \alpha_s^2}{512(2\pi)^3} \left\{ \left| (\lambda_{3H} g_t^S D(\hat{s}) + g_{tt}^S) F_\Delta^S + (g_t^S)^2 F_\square^{SS} + (g_t^P)^2 F_\square^{PP} \right|^2 \right. \\ &\quad + \left| (g_t^S)^2 G_\square^{SS} + (g_t^P)^2 G_\square^{PP} \right|^2 \\ &\quad \left. + \left| (\lambda_{3H} g_t^P D(\hat{s}) + g_{tt}^P) F_\Delta^P + g_t^S g_t^P F_\square^{SP} \right|^2 + \left| g_t^S g_t^P G_\square^{SP} \right|^2 \right\}. \end{aligned} \quad (4)$$

More explicitly in terms of each combination of couplings and ignoring the proportionality constant at the beginning of the equation, the above equation becomes

$$\begin{aligned} \frac{d\hat{\sigma}(gg \rightarrow HH)}{d\hat{t}} &\propto \lambda_{3H}^2 |D(\hat{s})|^2 \left[|F_\Delta^S|^2 (g_t^S)^2 + |F_\Delta^P|^2 (g_t^P)^2 \right] \\ &\quad + 2\lambda_{3H} g_t^S \Re \left\{ D(\hat{s}) \left[F_\Delta^S F_\square^{SS*} (g_t^S)^2 + (F_\Delta^S F_\square^{PP*} + F_\Delta^P F_\square^{SP*}) (g_t^P)^2 \right] \right\} \\ &\quad + \left[|F_\square^{SS}|^2 + |G_\square^{SS}|^2 \right] (g_t^S)^4 \\ &\quad + \left\{ 2\Re \left[F_\square^{SS} F_\square^{PP*} + G_\square^{SS} G_\square^{PP*} \right] + |F_\square^{SP}|^2 + |G_\square^{SP}|^2 \right\} (g_t^S)^2 (g_t^P)^2 \\ &\quad + \left[|F_\square^{PP}|^2 + |G_\square^{PP}|^2 \right] (g_t^P)^4 \\ &\quad + |F_\Delta^S|^2 (g_{tt}^S)^2 + |F_\Delta^P|^2 (g_{tt}^P)^2 \\ &\quad + 2g_{tt}^S \left[\lambda_{3H} g_t^S \Re(D) |F_\Delta^S|^2 + (g_t^S)^2 F_\Delta^S F_\square^{SS*} + (g_t^P)^2 F_\Delta^S F_\square^{PP*} \right] \\ &\quad + 2g_{tt}^P \left[\lambda_{3H} g_t^P \Re(D) |F_\Delta^P|^2 + g_t^S g_t^P F_\Delta^P F_\square^{SP*} \right], \end{aligned} \quad (5)$$

where $F_\Delta^P = F_\Delta^A$, $F_\square^{SP} = F_\square$, and $G_\square^{SP} = G_\square$ with F_Δ^A , F_\square and G_\square given in Appendix A.2 of Ref. [6] while $F_\square^{PP} = F_\square$, and $G_\square^{PP} = G_\square$ with F_\square and G_\square in Appendix A.3 of Ref. [6]. In

the heavy quark limit, one may have [6]

$$\begin{aligned}
F_{\Delta}^S &= +\frac{2}{3} + \mathcal{O}(\hat{s}/m_Q^2), & F_{\square}^{SS} &= -\frac{2}{3} + \mathcal{O}(\hat{s}/m_Q^2), & F_{\square}^{PP} &= +\frac{2}{3} + \mathcal{O}(\hat{s}/m_Q^2), \\
F_{\Delta}^P &= +1 + \mathcal{O}(\hat{s}/m_Q^2), & F_{\square}^{SP} &= -1 + \mathcal{O}(\hat{s}/m_Q^2), \\
G_{\square}^{SS} &= G_{\square}^{PP} = G_{\square}^{SP} = \mathcal{O}(\hat{s}/m_Q^2)
\end{aligned} \tag{6}$$

leading to large cancellation between the triangle and box diagrams.

The production cross section normalized to the corresponding SM cross section, with or without cuts, can be parameterized as follows:

$$\begin{aligned}
\frac{\sigma(gg \rightarrow HH)}{\sigma_{\text{SM}}(gg \rightarrow HH)} &= \lambda_{3H}^2 [c_1(s)(g_t^S)^2 + d_1(s)(g_t^P)^2] + \lambda_{3H} g_t^S [c_2(s)(g_t^S)^2 + d_2(s)(g_t^P)^2] \\
&+ [c_3(s)(g_t^S)^4 + d_3(s)(g_t^S)^2(g_t^P)^2 + d_4(s)(g_t^P)^4] \\
&+ \lambda_{3H} [e_1(s)g_t^S g_{tt}^S + f_1(s)g_t^P g_{tt}^P] + g_{tt}^S [e_2(s)(g_t^S)^2 + f_2(s)(g_t^P)^2] \\
&+ [e_3(s)(g_{tt}^S)^2 + f_3(s)g_t^S g_t^P g_{tt}^P + f_4(s)(g_{tt}^P)^2]
\end{aligned} \tag{7}$$

where the numerical coefficients $c_{1,2,3}(s)$, $d_{1,2,3,4}(s)$, $e_{1,2,3}$, and $f_{1,2,3,4}$ depend on s and experimental selection cuts. Upon our normalization, the ratio should be equal to 1 when $g_t^S = \lambda_{3H} = 1$ and $g_t^P = g_{tt}^{S,P} = 0$ or $c_1(s) + c_2(s) + c_3(s) = 1$. The coefficients $c_1(s)$ and $c_3(s)$ are for the SM contributions from the triangle and box diagrams, respectively, and the coefficient $c_2(s)$ for the interference between them.

Once we have the coefficients c_i, d_i, e_i , and f_i 's, the cross sections can be easily obtained for any combinations of couplings. Our first task is to obtain the dependence of the coefficients on the collider energy \sqrt{s} , Higgs decay channels, experimental cuts, etc.

III. BEHAVIOR OF THE CROSS SECTIONS

We first examine the behavior of each piece of cross sections versus energies. We show the coefficients c_i, d_i, e_i, f_i 's at $\sqrt{s} = 8, 14, 33, 100$ TeV in Table I and also in Fig. 1. The triangle diagram involves an s -channel Higgs-boson propagator. At center-of-mass energy $\sqrt{\hat{s}}$ considerably higher than M_H , it behaves like $1/\hat{s}$. Thus the triangle diagram decreases more rapidly than the box and contact diagrams, as reflected from the coefficients c_1 and d_1 when \sqrt{s} goes from 8 TeV to 100 TeV. The coefficients c_3, d_3 and d_4 associated with

TABLE I. The behavior of the coefficients $c_i(s)$, $d_i(s)$, $e_i(s)$, and $f_i(s)$ versus collider energy \sqrt{s} , see Eq. (7).

\sqrt{s} (TeV)	$c_1(s)$ [$\lambda_{3H}^2(g_t^S)^2$]	$c_2(s)$ [$\lambda_{3H}(g_t^S)^3$]	$c_3(s)$ [$(g_t^S)^4$]	$d_1(s)$ [$\lambda_{3H}^2(g_t^P)^2$]	$d_2(s)$ [$\lambda_{3H}g_t^S(g_t^P)^2$]	$d_3(s)$ [$(g_t^S)^2(g_t^P)^2$]	$d_4(s)$ [$(g_t^P)^4$]
8	0.300	-1.439	2.139	0.942	-6.699	14.644	0.733
14	0.263	-1.310	2.047	0.820	-5.961	13.348	0.707
33	0.232	-1.193	1.961	0.713	-5.274	12.126	0.690
100	0.208	-1.108	1.900	0.635	-4.789	11.225	0.683

\sqrt{s} (TeV)	$e_1(s)$ [$\lambda_{3H}g_t^S g_{tt}^S$]	$e_2(s)$ [$g_{tt}^S(g_t^S)^2$]	$e_3(s)$ [$(g_{tt}^S)^2$]	$f_1(s)$ [$\lambda_{3H}g_t^P g_{tt}^P$]	$f_2(s)$ [$g_{tt}^S(g_t^P)^2$]	$f_3(s)$ [$g_t^S g_t^P g_{tt}^P$]	$f_4(s)$ [$(g_{tt}^P)^2$]
8	1.460	-4.313	2.519	2.104	2.350	-7.761	3.065
14	1.364	-4.224	2.617	1.848	2.269	-6.886	3.769
33	1.281	-4.165	2.783	1.622	2.207	-6.033	5.635
100	1.214	-4.137	2.974	1.474	2.154	-5.342	10.568

the box diagram more or less remain the same as the energy goes up. On the other hand, the contact diagram involving the coefficients e_3 and f_4 increases with energy, in particular tremendous increases in f_4 . It is easy to see that the contact diagram is dim-5 and obviously grows with energy. At certain high enough energy, it may upset unitarity.

We can examine the validity of the anomalous $ttHH$ contact coupling by projecting out the leading partial-wave coefficient for the scattering $t\bar{t} \rightarrow HH$. At high energy, the amplitude

$$i\mathcal{M}(t\bar{t} \rightarrow HH) \sim g_{tt}^S \frac{m_t \sqrt{\hat{s}}}{v^2}.$$

The leading partial-wave coefficient is given by

$$a_0 = \frac{1}{64\pi} \int_{-1}^1 d(\cos\theta) P_0(\cos\theta) (i\mathcal{M}) = g_{tt}^S \frac{m_t \sqrt{\hat{s}}}{32\pi v^2}.$$

Requiring $|a_0| < 1/2$ for unitarity we obtain

$$\sqrt{\hat{s}} \leq \frac{17.6}{g_{tt}^S} \text{ TeV}.$$

Therefore, the anomalous $ttHH$ contact term can be safely applied at the LHC.

To some extent we have understood the behavior of the triangle, box, and contact diagrams with the center-of-mass energy, which is kinematically equal to the invariant mass

M_{HH} of the Higgs-boson pair. One can then use M_{HH} to enhance or reduce the relative contributions of triangle or box diagrams. The higher the M_{HH} the relatively larger proportion comes from the box and contact diagrams. Since M_{HH} correlates with the boost energy of each Higgs boson, a more energetic Higgs boson will decay into a pair of particles, which have a smaller angular separation between them than a less energetic Higgs boson. Therefore, the angular separation ΔR_{ij} between the decay products i, j is another useful kinematic variable to separate the contributions among the triangle, box, and contact diagrams.

IV. NUMERICAL ANALYSIS

The Lagrangian in Eq. (1) consists of five parameters: the scalar and pseudoscalar parts of the top-Yukawa coupling $g_t^{S,P}$, the scalar and pseudoscalar parts of the anomalous contact coupling $g_{tt}^{S,P}$, and the Higgs trilinear coupling λ_{3H} . In order to facilitate the presentation and understanding of the physics, we study a few scenarios:

1. **CPC1**—the top-Yukawa coupling involves only the scalar part and the scale in the anomalous contact coupling is very large – only g_t^S and λ_{3H} are relevant. The relevant coefficients are c_1 , c_2 , and c_3 .
2. **CPC2**—the top-Yukawa and the anomalous contact couplings involve only the scalar part – g_t^S , g_{tt}^S , and λ_{3H} are relevant. The relevant coefficients are c_1 , c_2 , c_3 , e_1 , e_2 , and e_3 .
3. **CPV1**—the top-Yukawa coupling involves both the scalar and pseudoscalar parts – g_t^S , g_t^P , and λ_{3H} are relevant. The relevant coefficients are c_1 , c_2 , c_3 , d_1 , d_2 , d_3 , and d_4 .

A. CPC1: g_t^S and λ_{3H}

This is the simplest scenario to investigate the variation of the triangle and box diagrams with respect to changes in the Yukawa and trilinear couplings. The corresponding coefficients in Eq. (7) are c_1, c_2, c_3 . We let the Higgs boson pair decay into

$$HH \rightarrow (\gamma\gamma) (b\bar{b}) .$$

Note that if the process is studied without detector simulation, the distributions for other decay channels, like $b\bar{b}\tau\tau$ or $\gamma\gamma\tau\tau$ would be the same. Nevertheless, the resolutions for b , τ , and γ are quite different in detectors, and so are the backgrounds considered for each decay channel. In the following, we focus on the $\gamma\gamma b\bar{b}$ channel, which has been considered in a number of works.

We use MADGRAPH v.5 [13] with parton showering by Pythia v.6 [14] and detector simulations using Delphes v.3[15]. We have verified that the coefficients $c_{1,2,3}$ using the default, ATLAS, and CMS templates inside Delphes v.3 are within 10% of one another. From now on we employ the ATLAS template in detector simulations. We show the coefficients in Table II. We will come back to this table a bit later.

We first look at the distribution of events versus the invariant mass of the Higgs-boson pair via $HH \rightarrow \gamma\gamma b\bar{b}$ in Fig. 2 (upper panel) and versus the transverse momentum of the photon pair $p_{T,\gamma\gamma}$ (lower panel). In principle, up to detector simulations and higher-order emissions, the transverse momentum distribution of the photon pair is the same as that of the $b\bar{b}$ pair. The triangle diagram (red line) peaks at the lower invariant mass and decreases with $M_{\gamma\gamma b\bar{b}}$, because of the s -channel Higgs propagator. The box diagram (skyblue line), on the other hand, is larger than the triangle diagram at high invariant mass. The (darkblue) SM line represents the whole contributions including the destructive interference between the triangle and box diagrams. Similar behavior can be seen in the p_T distribution of the photon pair.

Next, we look at the distributions versus $\Delta R_{\gamma\gamma}$ and $\Delta R_{b\bar{b}}$ in Fig. 3. The lines are the same as in Fig. 2. As we have explained in the previous section, $\Delta R_{\gamma\gamma}$ and $\Delta R_{b\bar{b}}$ between the decay products of each Higgs boson are useful variables to separate the triangle and box contributions. The angular distribution ΔR between the two decay products of each Higgs boson correlates with the energy of the Higgs boson, which in turns correlates with the invariant of the Higgs-boson pair. The higher the invariant mass, the more energetic the Higgs boson will be, and the smaller the angular separation between the decay products will be. Therefore, the triangle diagram has wider separation than the box diagram.

It is clear that the distributions of $\Delta R_{\gamma\gamma}$ and $\Delta R_{b\bar{b}}$ have similar behavior within uncertainties. The box diagram and also the SM, which is dominated by the box contribution, have a peak at $\Delta R_{\gamma\gamma}$ or $\Delta R_{b\bar{b}}$ less than 2.0, while the triangle diagram prefers to have the majority at larger $\Delta R_{\gamma\gamma}$ or $\Delta R_{b\bar{b}}$, say between 2 and 3. We therefore come up with (i)

$\Delta R_{\gamma\gamma} > 2$ (< 2), (ii) $\Delta R_{b\bar{b}} > 2$ (< 2), and (iii) $\Delta R_{\gamma\gamma} > 2$ and $\Delta R_{b\bar{b}} > 2$ (both < 2) to enrich the sample of triangle (box) contribution. In the following, we use ΔR to denote either $\Delta R_{\gamma\gamma}$ or $\Delta R_{b\bar{b}}$, unless stated distinctively.

We can now look at Table II, where the coefficients for the ratio of the cross sections $\sigma(gg \rightarrow HH)/\sigma_{\text{SM}}(gg \rightarrow HH)$ as in Eq. (7) are shown. In the **CPC1** case, the relevant coefficients are c_1 , c_2 , and c_3 in which c_1 is induced by the triangle diagram, c_3 by the box diagram, and c_2 by the interference between them. The values appearing in the row of “No Cuts” are the same as those in Table I for $\sqrt{s} = 14$ TeV. In the same Table, we also show the coefficients obtained after applying the angular-separation cuts of $\Delta R > 2$ or < 2 and both $\Delta R_{\gamma\gamma, b\bar{b}} > 2$ or < 2 . It is clear that $\Delta R_{\gamma\gamma} > 2$ (< 2) enriches the triangle-diagram (box-diagram) contribution. Similar is true for $\Delta R_{b\bar{b}} > 2$ (< 2). Further enhancement of triangle diagram can be obtained with both $\Delta R_{\gamma\gamma} > 2$ and $\Delta R_{b\bar{b}} > 2$, and vice versa for box diagram.

In the following, we investigate the sensitivity in the parameter space (g_t^S, λ_{3H}) that one can reach at the 14 TeV with 3000 fb^{-1} luminosity by using the measurements of cross sections in various kinematical regions. Since we have found that the triangle and box contributions can be distinguished using the ΔR cuts, we make use of the measured cross sections in the kinematical regions separated by these cuts.

There are two issues that we have to considered when we take the measured cross sections in the kinematical regions. First, the SM backgrounds for the decay channel that we consider, and second, the Next-to-Leading-Order (NLO) corrections [16]. It was shown in Ref. [16] that the NLO and NNLO corrections can be as large as 100% with uncertainty of order 10–20%. The SM backgrounds, on the other hand, can be estimated with uncertainties less than the NNLO corrections. We therefore adopt an approach that the signal cross sections (after background subtraction) are measured with uncertainties of order 25–50%.

About the signal cross sections, the first and the second columns of Table III show the SM cross sections for the process $pp \rightarrow HH \rightarrow \gamma\gamma b\bar{b}$ with detector simulations under various cuts at the 14 TeV LHC. We have taken account of the SM NLO cross section $\sigma_{\text{SM}}(pp \rightarrow HH) \simeq 34 \text{ fb}$, the Higgs branching fractions, and both the photon and b -quark reconstruction efficiencies with angular-separation cuts of $\Delta R_{b\bar{b}, \gamma\gamma}$. In various kinematical regions depending on the angular cuts, the cross sections range from $\sim 0.001 \text{ fb}$ to $\sim 0.05 \text{ fb}$. With an integrated luminosity of 3000 fb^{-1} , we expect of order 30 signal events when the

cross section is 0.01 fb. An estimate of the statistical error is given by the square root of the number of events \sqrt{N} , which is then roughly 20% of the total number. Taking into account the uncertainty of order 10 – 20% from NLO and NNLO corrections, in this work, we use a total uncertainty of 25 – 50% in the signal cross section in the estimation of sensitivity of the couplings. Our approach is more or less valid except for the case in which both the $\Delta R_{b\bar{b}} > 2$ and $\Delta R_{\gamma\gamma} > 2$ cuts are imposed simultaneously. It would be challenging to measure this size of cross section only in the $HH \rightarrow \gamma\gamma b\bar{b}$ mode and one may need to combine the measurements in different Higgs-decay channels. Or, one may rely on the future colliders such as a 100 TeV pp machine with larger cross sections and/or higher luminosities.

In Fig. 4, we show the contour lines of $\sigma(gg \rightarrow HH)/\sigma_{\text{SM}}(gg \rightarrow HH) = 0.5$ and 1.5 with the Higgs boson pair decaying into $(\gamma\gamma)(b\bar{b})$. In each panel, we assume three measurements of the ratios corresponding to no cuts (orange lines), $\Delta R > 2$ (dashed black lines), and $\Delta R < 2$ (solid black lines): here ΔR represents $\Delta R_{\gamma\gamma}$ (upper left), $\Delta R_{b\bar{b}}$ (upper right), or $\Delta R_{\gamma\gamma, b\bar{b}}$ (lower). Therefore, for example, if the no-cuts cross section ratio is measured to be consistent with the SM prediction within 50% error, any points in the two bands bounded by the two pairs of orange lines are allowed. In each band, a rather wide range of g_t^S and λ_{3H} is allowed although they are correlated. Suppose we only make one measurement of the cross section without or with a cut on ΔR , we would not be able to pin down useful values for g_t^S and λ_{3H} . However, since the shape of the three bands are not exactly the same, we can make use of three simultaneous measurements in order to obtain more useful information for the couplings g_t^S and λ_{3H} .

In the upper-left panel of Fig. 4, we suppose that one can make three measurements of cross sections: with no cuts, $\Delta R_{\gamma\gamma} > 2$, and $\Delta R_{\gamma\gamma} < 2$. We assume that the measurements agree with the SM predictions within 25% or 50% uncertainty. The region of parameter space in (g_t^S, λ_{3H}) bounded by the three measurements is shown by the lighter pink region for 50% uncertainty and darker pink region for 25% uncertainty. Similarly the upper-right panel is for the regions with the $\Delta R_{b\bar{b}}$ cut. In the lower panel, we show the regions with the combined cuts of $\Delta R_{\gamma\gamma}$ and $\Delta R_{b\bar{b}}$: both larger than or smaller than 2. The implications from the measurements are very significant. First, all panels show that g_t^S is significantly away from zero if one can simultaneously measure the cross sections (no matter with 25% or 50% uncertainties) with no cuts, $\Delta R_{\gamma\gamma} > 2$, and $\Delta R_{\gamma\gamma} < 2$; and similarly for $\Delta R_{b\bar{b}}$ and using both distributions. Second, as shown in the lower panel, the value for λ_{3H} is statistically

distinct from zero if one measures the cross sections with a 25% uncertainty. This is achieved by using both $\Delta R_{\gamma\gamma}$ and $\Delta R_{b\bar{b}} > 2$ or < 2 .

We can repeat the exercise with the measured cross sections being multiples of the SM predictions. We show the corresponding 25% and 50% regions in Fig. 5 for $\sigma/\sigma_{\text{SM}} = 0.5, 1, 2, 5, 10$. Only with both $\Delta R_{\gamma\gamma}$ and $\Delta R_{b\bar{b}}$, one can really tell if λ_{3H} is significantly distinct from zero.

If the top-Yukawa coupling can be constrained more effectively by Higgs production, by $t\bar{t}H$ production, or by single top with Higgs production in the future measurements, say $g_t^S = 1 \pm 0.1$ (10% uncertainty), it can help pinning down the acceptable range of λ_{3H} . However, even in this case, we emphasize the importance of simultaneous independent measurements, as illustrated in the following argument. In the limit of $g_t^S = 1$, the ratio of the cross sections is given by

$$\frac{\sigma(gg \rightarrow HH)}{\sigma_{\text{SM}}(gg \rightarrow HH)} = c_1(s) \lambda_{3H}^2 + c_2(s) \lambda_{3H} + c_3(s). \quad (8)$$

Suppose $\sigma(gg \rightarrow HH)$ is measured to be the same as $\sigma_{\text{SM}}(gg \rightarrow HH)$ and then, using the relation $c_1(s) + c_2(s) + c_3(s) = 1$, one may find the two solutions for λ_{3H} : 1 or $-c_2(s)/c_1(s) - 1$. For example, one may have $\lambda_{3H} = 1$ or 3.98 at most if only the no-cuts ratio is measured. Therefore, one cannot determine λ_{3H} uniquely with only one measurement even when the measurement is very precise and the exact value of g_t^S is known. It is unlikely to resolve this two-fold ambiguity at the LHC even we assume the three measurements of the ratios, as shown in Fig. 4. Also, the situation remains the same at the 100 TeV pp machine in which we have $\lambda_{3H} = 1$ or 4.33 in the no-cuts case when $\sigma(gg \rightarrow HH) = \sigma_{\text{SM}}(gg \rightarrow HH)$, see Table I and Fig. 21. If a future e^+e^- linear collider and/or the 100 TeV pp machine are operating in the era of the high-luminosity LHC, combined efforts are desirable to determine the value of λ_{3H} uniquely [17].

B. CPC2: g_t^S , λ_{3H} , and g_{tt}^S

This is the scenario that involves all scalar-type couplings in the triangle, box, and contact diagrams. The corresponding coefficients in Eq. (7) are $c_1, c_2, c_3, e_1, e_2, e_3$. Results at the detector level using the ATLAS template in Delphes v.3 are shown in Table II.

We first examine the cross section versus one input parameter at a time, shown in Fig. 6, while keeping the two parameters at their corresponding SM values. In the upper-left panel for $\sigma/\sigma_{\text{SM}}$ versus λ_{3H} , the lowest point occurs at $\lambda_{3H} \approx 2.5$ when the interference term strongly cancels the triangle and box diagrams. Then the ratio increases from the lowest point on either side of $\lambda_{3H} \approx 2.5$. Negative λ_{3H} s give constructive interference while positive λ_{3H} s give destructive interference. One may observe similar behavior when g_{tt}^S is varied as shown in the lower panel. Taking $\lambda_{3H} = g_t^S = 1$,

$$\frac{\sigma(gg \rightarrow HH)}{\sigma_{\text{SM}}(gg \rightarrow HH)} = e_3(s) (g_{tt}^S)^2 + [e_2(s) + e_1(s)] g_{tt}^S + 1. \quad (9)$$

Since $e_1(s) > 0$ and $e_2(s) < 0$, we see that the contact diagram interferes constructively with the triangle diagram but destructively with the box diagram. The dominance of the box diagram leads to the totally destructive interference when $g_{tt}^S > 0$, resulting in the minimum at $g_{tt}^S \approx 0.5$.

We show contours for the ratio $\sigma/\sigma_{\text{SM}} = 0.5, 1.5$ in the plane of (λ_{3H}, g_t^S) (upper-left), (λ_{3H}, g_{tt}^S) (upper-right), and (g_t^S, g_{tt}^S) (lower) in Fig. 7. The dashed lines denoted by -50% is for $\sigma/\sigma_{\text{SM}} = 0.5$ and those by $+50\%$ for $\sigma/\sigma_{\text{SM}} = 1.5$. In the upper-left panel in the plane of (λ_{3H}, g_t^S) , we show contours for $g_{tt}^S = 0, 1$. The $g_{tt}^S = 0$ is the same as the SM so that the contours are exactly the same as in Fig. 4, while with $g_{tt}^S = 1$, the contact diagram contributes significantly to the cross section, so that the contours shift more to negative (positive) λ_{3H} for positive (negative) g_t^S . In the upper-right panel, where we show the contours in the plane of (λ_{3H}, g_{tt}^S) , the g_{tt}^S negatively correlates with λ_{3H} because $e_1(s) > 0$. In the lower panel, where we fix $\lambda_{3H} = 1$, somewhat nontrivial correlation between g_t^S and g_{tt}^S exists.

We use the same tools as in the **CPC1** case to investigate the decay channel $HH \rightarrow \gamma\gamma b\bar{b}$ with parton showering and detector simulations. We first show the invariant mass ($M_{\gamma\gamma b\bar{b}}$) distribution of the Higgs-boson pair and the transverse momentum distribution of the photon pair in Fig. 8. The figure clearly illustrates the behavior of each contributing diagram. The triangle diagram (red lines) peaks at the lower invariant mass and decreases with $M_{\gamma\gamma b\bar{b}}$, because of the s -channel Higgs propagator. Then followed by the box diagram (skyblue lines) which is larger than the triangle diagram at high invariant mass. The (darkblue) SM line represents the contributions from the triangle and box diagram including the destructive

interference between them. These three distributions are the same as in the **CPC1** case. The contact diagram (green lines) shows similar behavior as the box diagram (skyblue lines) at low $M_{\gamma b\bar{b}}$ and $P_{T_{\gamma\gamma}}$ but with higher and larger tails. The grey and magenta lines represent the full contributions including the destructive and constructive interferences among the triangle, box, and contact diagrams when $g_{tt}^S = +1$ and $g_{tt}^S = -1$, respectively. The contact diagram is the largest at the high invariant mass. It demonstrates what we describe earlier that the contact diagram grows with energy.

We show the angular distributions $\Delta R_{\gamma\gamma}$ and $\Delta R_{b\bar{b}}$ between the two decay products of each Higgs boson in Fig. 9. The lines are the same as in Fig. 8. Similar to the **CPC1** case, the higher the invariant mass, the more energetic the Higgs boson, and the smaller the angular separation between the decay products will be. Therefore, triangle diagram (red lines) has the widest separation, then followed by the box diagram (skyblue lines), and finally the contact diagram (green lines) has the smallest angular separation. We come up with the similar cuts as in the **CPC1** case: ΔR larger or smaller than 2 to discriminate the triangle, box, and contact diagrams. We show in Table II the coefficients $c_1, c_2, c_3, e_1, e_2, e_3$ such that the ratio of cross sections to the SM predictions can be given by Eq. (7).

Similar to what we have done for **CPC1**, we can make use of three simultaneous measurements of cross sections with no cuts, $\Delta R > 2$, and $\Delta R < 2$. We show the region of parameter space that we can obtain using $\Delta R_{\gamma\gamma}$ (upper panels), $\Delta R_{b\bar{b}}$ (middle panels), and $\Delta R_{\gamma\gamma}$ and $\Delta R_{b\bar{b}}$ (lower panels) in the plane of (λ_{3H}, g_t^S) in Fig. 10. Those on the left are for $g_{tt}^S = 1$ while those on the right are for $g_{tt}^S = -1$. Similarly, we show the parameter space in the plane of (λ_{3H}, g_t^S) in Fig. 11 and in the plane of (g_t^S, g_{tt}^S) in Fig. 12.

C. **CPV1**: g_t^S, g_t^P , and λ_{3H}

In this scenario, we entertain the possibility that the top Yukawa coupling allows an imaginary part. In most of the measurements of the Higgs boson production cross sections, for example, Higgs boson production cross section via gluon fusion and $t\bar{t}H$ production, both the real and imaginary parts of the coupling come in the form $|g_t^S|^2 + |g_t^P|^2$, therefore one cannot tell the phase in the coupling¹. The relevant coefficients for this **CPV1** scenario are

¹ Single top plus Higgs production. on the other hand, has some chances to isolate the phase of the Yukawa coupling [18].

$c_1, c_2, c_3, d_1, d_2, d_3, d_4$. They are shown in Table II at both levels of no detector simulation (no cuts) and detector simulations (ATLAS).

We first show the variations of cross sections versus λ_{3H} with some fixed values of g_t^S and g_t^P in Fig. 13². Also, the contours for the ratio $\sigma/\sigma_{\text{SM}} = 1$ in the plane of (λ_{3H}, g_t^S) (upper-left), (λ_{3H}, g_t^P) (upper-right), and (g_t^S, g_t^P) (lower) for a few values of the third parameter are shown in Fig. 14.

Similar to previous two scenarios, we use the same tools to analyze the decay channel $HH \rightarrow \gamma\gamma b\bar{b}$ with parton showering and detector simulations. We show the invariant mass $M_{\gamma\gamma b\bar{b}}$ and $p_{T\gamma\gamma}$ in Fig. 15, and the angular distributions $\Delta R_{\gamma\gamma}$ and $\Delta R_{b\bar{b}}$ between the two decay products of each Higgs boson in Fig. 16.

The terms by the triangle diagram (proportional to c_1 and d_1 in red and orange lines, respectively) give the widest separation among all the terms. The terms by the box diagram (proportional to c_3 and d_4 in skyblue and blue lines, respectively) give smaller angular separation. The full set of diagrams at the SM values (darkblue lines) and at $g_t^S = g_t^P = 1/\sqrt{2}$ (grey lines) give similar results as the box diagram.

Similar to the **CPC1** and **CPC2** cases, we use the cuts ΔR larger or smaller than 2 to discriminate the triangle and box diagrams. We show in Table II the coefficients $c_1, c_2, c_3, d_1, d_2, d_3, d_4$, which are relevant ones in the **CPV1** scenario, such that the ratio of cross sections to the SM predictions can be obtained by Eq. (7). We show the region of parameter space that we can obtain using $\Delta R_{\gamma\gamma}$, $\Delta R_{b\bar{b}}$, and $\Delta R_{\gamma\gamma}$ and $\Delta R_{b\bar{b}}$ in the plane of (g_t^S, g_t^P) in Fig. 17, in the plane of (λ_{3H}, g_t^P) in Fig. 18, and in the plane of (λ_{3H}, g_t^S) in Fig. 19.

D. 100 TeV Prospect

All the results represented for the 14 TeV run were obtained by manipulating the coefficients represented in Table II. We represent the coefficients $c_{1,2,3}, d_{1,2,3,4}, e_{1,2,3}$ for the 100 TeV pp machine in Table IV. Just for illustrations, we show the distributions of the invariant mass $M_{\gamma\gamma b\bar{b}}$ and angular separation $\Delta R_{\gamma\gamma}$ for the **CPC1** case at the 100 TeV machine in Fig. 20. We found that the behavior of the distributions at 100 TeV is very similar to those at 14 TeV. Therefore, the kinematic regions of interests separated by ΔR can be taken to

² We note that the lines are the same for the negative values of g_t^P since the cross section contains only the $(g_t^P)^2$ and $(g_t^P)^4$ terms.

be the same as 14 TeV. We can make simultaneous measurements of cross sections at 100 TeV pp machine to isolate the Higgs trilinear coupling. We show the sensitivity regions of parameter space in the **CPC1** case at the 100 TeV pp machine in Fig. 21. The regions are very similar to those in 14 TeV, though not exactly the same. Sensitivity reach for each coupling in other cases can be obtained by similar methods with the assumed luminosity.

V. CONCLUSIONS

In this work, we have studied the behavior of Higgs-boson pair production via gluon fusion at the 14 TeV LHC and the 100 TeV pp machine. We have performed a model-independent study with heavy degrees of freedom being integrated out and resulting in possible modifications of the top-Yukawa coupling, Higgs trilinear coupling, and a new contact $ttHH$ coupling, as well as the potential CP-odd component in the Yukawa and contact couplings. We have identified useful variables – the angular separation between the decay products of the Higgs boson – to discriminate among the contributions from the triangle, box, and contact diagrams. We have successfully demonstrated that with three simultaneous measurements of the Higgs-pair production cross sections, defined by the kinematic cuts, one can statistically show a nonzero value for the Higgs trilinear coupling λ_{3H} if we can measure the cross sections with less than 25% uncertainty. This is the key result of this work.

We also offer the following comments with regards to our findings.

1. The triangle diagram, which contains an s -channel Higgs propagator, does not increase as much as the box diagram or the contact diagram with the center-of-mass energy $\sqrt{\hat{s}}$. This explains why the opening angle ($\Delta R_{\gamma\gamma}$ or ΔR_{bb}) in the decay products of each Higgs boson is a useful variable to separate between the triangle and the box diagram. Thus, it helps to isolate the Higgs trilinear coupling λ_{3H} .
2. The contact diagram contains a dim-5 operator $ttHH$, which actually breaks the unitarity at about $\sqrt{\hat{s}} \sim 17.6/g_{tt}^S$ TeV. This implies that it could become dominant at high invariant mass.
3. Suppose we take a measurement of cross sections, we can map out the possible region of parameter space. Since in different kinematic regions the regions of parameter space

are mapped out differently, such that simultaneous measurements can map out the intersected regions. With measurement uncertainties less than 25% one can statistically show a nonzero value for the Higgs trilinear coupling.

4. We found that the behavior of the distributions of the invariant mass $M_{\gamma\gamma b\bar{b}}$ and angular separation $\Delta R_{\gamma\gamma}$ or $\Delta R_{b\bar{b}}$ at 14 TeV are very similar to those at 100 TeV. We can then use the same method as in 14 TeV to isolate the Higgs trilinear coupling.
5. It is difficult, if not impossible, to determine the Higgs trilinear coupling uniquely at the LHC and 100 TeV pp machine even in the simplest case assuming very high luminosity and precise independent input for the top-Yukawa coupling. We suggest to combine the LHC results with information which can be obtained at a future e^+e^- linear collider.
6. If the couplings deviate from their SM values, the Higgs-boson pair production cross section can easily increase by an order of magnitude. For example, in the **CPC2** case, $\sigma/\sigma_{\text{SM}} > 10$ for $\lambda_{3H} > 9$ or < -4 when $g_t^S = 1$ and $g_{tt}^S = 0$, $g_t^S > 1.7$ or < -1.3 when $\lambda_{3H} = 1$ and $g_{tt}^S = 0$, and $g_{tt}^S > 2.6$ or < -1.4 when $\lambda_{3H} = g_t^S = 1$: see Fig. 6. The cross section larger than the SM prediction may reveal the new physics hidden behind the SM and we can have better prospect to measure the Higgs self coupling at the LHC.

ACKNOWLEDGMENT

This work was supported by the National Science Council of Taiwan under Grants No. 102-2112-M-007-015-MY3, and by the National Research Foundation of Korea (NRF) grant (No. 2013R1A2A2A01015406).

Appendix A

In Table III, we show the SM cross sections for $pp \rightarrow HH \rightarrow \gamma\gamma b\bar{b}$ at the 14 TeV LHC with and without angular-separation cuts. Note that the cross section before applying cuts is about 0.09 fb. In the region of $\Delta R_{\gamma\gamma} > 2 (< 2)$, the cross section is 0.018 fb (0.046 fb) where it is dominated by the triangle (box) diagram. The ratio is about 1 : 2.6. We also show the

cross sections for the 100 TeV pp machine, and the corresponding ratio is about 1 : 2.7. It shows the fact that the triangle diagram is more suppressed because of the s -channel Higgs propagator at higher energy. In the regions of $\Delta R_{b\bar{b}}$ larger and smaller than 2, the ratios are 1 : 5 and 1 : 5.3 at the 14 TeV LHC and the 100 TeV pp machine, respectively.

As we have promised, we are going to comment on the $HH \rightarrow \tau^+\tau^-b\bar{b}$ decay mode. This mode has the obvious advantage of a larger branching ratio than the $\gamma\gamma b\bar{b}$ mode, but the identification efficiency and momentum measurements of τ leptons are much weaker than photons. In Table III, we show the SM cross sections for $pp \rightarrow HH \rightarrow \tau^+\tau^-b\bar{b}$ at the 14 TeV LHC with and without angular-separation cuts. Taking into account the branching ratios, and the identification and selection efficiencies, the event rates of $\gamma\gamma b\bar{b}$ is about one third to one half of the $\tau^+\tau^-b\bar{b}$ mode, except when only the ΔR_{bb} cut is applied. So far, we have not mentioned the invariant mass of the photon pair or tau-lepton pair in reconstructing the Higgs boson mass. Indeed, experimentally one needs to reconstruct the photon pair or the tau-lepton pair at the Higgs boson mass in order to suppress the continuum background. The photon pair is obviously superior in reconstructing the invariant mass than the tau-lepton pair. Therefore, we expect the $\gamma\gamma b\bar{b}$ mode may perform better than the $\tau^+\tau^-b\bar{b}$ mode.

-
- [1] G. Aad *et al.* [ATLAS Collaboration], Phys. Lett. B **716**, 1 (2012) [arXiv:1207.7214 [hep-ex]].
 - [2] S. Chatrchyan *et al.* [CMS Collaboration], Phys. Lett. B **716**, 30 (2012) [arXiv:1207.7235 [hep-ex]].
 - [3] See for example, K. Cheung, J. S. Lee and P. -Y. Tseng, JHEP **1305**, 134 (2013) [arXiv:1302.3794 [hep-ph]].
 - [4] K. Cheung, J. S. Lee and P. Y. Tseng, Phys. Rev. D **90**, no. 9, 095009 (2014) [arXiv:1407.8236 [hep-ph]].
 - [5] P. W. Higgs, Phys. Rev. Lett. **13**, 508 (1964); F. Englert and R. Brout, Phys. Rev. Lett. **13**, 321 (1964); G. S. Guralnik, C. R. Hagen and T. W. B. Kibble, Phys. Rev. Lett. **13**, 585 (1964).
 - [6] T. Plehn, M. Spira and P. M. Zerwas, Nucl. Phys. B **479**, 46 (1996) [Erratum-ibid. B **531**, 655 (1998)] [hep-ph/9603205].
 - [7] J. Baglio, A. Djouadi, R. Grber, M. M. Mhleitner, J. Quevillon and M. Spira, JHEP **1304**,

- 151 (2013) [arXiv:1212.5581 [hep-ph]].
- [8] V. Barger, L. L. Everett, C. B. Jackson and G. Shaughnessy, *Phys. Lett. B* **728**, 433 (2014) [arXiv:1311.2931 [hep-ph]]; E. Asakawa, D. Harada, S. Kanemura, Y. Okada and K. Tsumura, *Phys. Rev. D* **82**, 115002 (2010) [arXiv:1009.4670 [hep-ph]].
- [9] K. Nishiwaki, S. Niyogi and A. Shivaji, *JHEP* **1404**, 011 (2014) [arXiv:1309.6907 [hep-ph]]; M. Gouzevitch, A. Oliveira, J. Rojo, R. Rosenfeld, G. P. Salam and V. Sanz, *JHEP* **1307**, 148 (2013) [arXiv:1303.6636 [hep-ph]]; F. Goertz, A. Papaefstathiou, L. L. Yang and J. Zurita, *JHEP* **1306**, 016 (2013) [arXiv:1301.3492 [hep-ph]]; M. J. Dolan, C. Englert and M. Spannowsky, *JHEP* **1210**, 112 (2012) [arXiv:1206.5001 [hep-ph]]; A. Azatov, R. Contino, G. Panico and M. Son, arXiv:1502.00539 [hep-ph]; R. Contino, M. Ghezzi, M. Moretti, G. Panico, F. Piccinini and A. Wulzer, *JHEP* **1208**, 154 (2012) [arXiv:1205.5444 [hep-ph]].
- [10] C. R. Chen and I. Low, *Phys. Rev. D* **90**, no. 1, 013018 (2014) [arXiv:1405.7040 [hep-ph]].
- [11] S. Dawson, E. Furlan and I. Lewis, *Phys. Rev. D* **87**, no. 1, 014007 (2013) [arXiv:1210.6663 [hep-ph]]; M. Gillioz, R. Grober, C. Grojean, M. Muhlleitner and E. Salvioni, *JHEP* **1210** (2012) 004 [arXiv:1206.7120 [hep-ph]]; V. Barger, L. L. Everett, C. B. Jackson, A. Peterson and G. Shaughnessy, *Phys. Rev. Lett.* **114**, 011801 (2015) [arXiv:1408.0003 [hep-ph]]; M. J. Dolan, C. Englert and M. Spannowsky, *Phys. Rev. D* **87** (2013) 5, 055002 [arXiv:1210.8166 [hep-ph]]; G. D. Kribs and A. Martin, *Phys. Rev. D* **86**, 095023 (2012) [arXiv:1207.4496 [hep-ph]]; A. Arhrib, R. Benbrik, C. H. Chen, R. Guedes and R. Santos, *JHEP* **0908**, 035 (2009) [arXiv:0906.0387 [hep-ph]]; C. O. Dib, R. Rosenfeld and A. Zerwekh, *JHEP* **0605**, 074 (2006) [hep-ph/0509179]; R. Grober and M. Muhlleitner, *JHEP* **1106**, 020 (2011) [arXiv:1012.1562 [hep-ph]].
- [12] C. Han, X. Ji, L. Wu, P. Wu and J. M. Yang, *JHEP* **1404**, 003 (2014) [arXiv:1307.3790 [hep-ph]]; U. Ellwanger, *JHEP* **1308**, 077 (2013) [arXiv:1306.5541 [hep-ph]]; J. Cao, Z. Heng, L. Shang, P. Wan and J. M. Yang, *JHEP* **1304**, 134 (2013) [arXiv:1301.6437 [hep-ph]].
- [13] MADGRAPH: J. Alwall, M. Herquet, F. Maltoni, O. Mattelaer and T. Stelzer, *JHEP* **1106**, 128 (2011) [arXiv:1106.0522 [hep-ph]].
- [14] J. Alwall and the CP3 development team, *The MG/ME Pythia-PGS package*; the Madgraph at <http://madgraph.hep.uiuc.edu/>; Pythia at <https://pythia6.hepforge.org/>; and PGS at <http://www.physics.ucdavis.edu/~conway/research/software/pgs/pgs4-general.htm>.
- [15] J. de Favereau *et al.* [DELPHES 3 Collaboration], *JHEP* **1402**, 057 (2014) [arXiv:1307.6346

[hep-ex]].

[16] D. de Florian and J. Mazzitelli, Phys. Rev. Lett. **111**, 201801 (2013) [arXiv:1309.6594 [hep-ph]].

[17] J. Chang, K. Cheung, J. S. Lee and C. T. Lu, in preparation.

[18] J. Chang, K. Cheung, J. S. Lee and C. T. Lu, JHEP **1405**, 062 (2014) [arXiv:1403.2053 [hep-ph]].

TABLE II. **14 TeV LHC:** The coefficients for the ratio of the cross sections $\sigma(gg \rightarrow HH)/\sigma_{\text{SM}}(gg \rightarrow HH)$ as in Eq. (7) with and without the angular-separation cuts of $\Delta R_{\gamma\gamma} >$ or < 2 ; $\Delta R_{b\bar{b}} >$ or < 2 ; and $\Delta R_{\gamma\gamma}$ and $\Delta R_{b\bar{b}}$ both > 2 or < 2 . The relevant coefficients for the **CPC1** scenario are c_1, c_2, c_3 ; those for the **CPC2** scenario are $c_1, c_2, c_3, e_1, e_2, e_3$; and those for the **CPV1** scenario are $c_1, c_2, c_3, d_1, d_2, d_3, d_4$. Results are at the detector level using the ATLAS template in Delphes v.3.

$\sqrt{s} : 14 \text{ TeV}$	$c_1(s)$	$c_2(s)$	$c_3(s)$	$e_1(s)$	$e_2(s)$	$e_3(s)$
Cuts	$[\lambda_{3H}^2 (g_t^S)^2]$	$[\lambda_{3H} (g_t^S)^3]$	$[(g_t^S)^4]$	$[\lambda_{3H} g_t^S g_{tt}^S]$	$[g_{tt}^S (g_t^S)^2]$	$[(g_{tt}^S)^2]$
No Cuts	0.263	-1.31	2.047	1.364	-4.224	2.617
$\Delta R_{\gamma\gamma} > 2$	0.480	-2.001	2.521	1.859	-4.782	2.422
$\Delta R_{\gamma\gamma} < 2$	0.132	-0.838	1.706	1.057	-3.743	2.596
$\Delta R_{b\bar{b}} > 2$	0.625	-2.576	2.951	2.341	-5.525	2.731
$\Delta R_{b\bar{b}} < 2$	0.143	-0.800	1.657	0.965	-3.673	2.497
$\Delta R_{b\bar{b}} > 2 \ \& \ \Delta R_{\gamma\gamma} > 2$	0.713	-3.020	3.307	2.844	-5.907	2.704
$\Delta R_{b\bar{b}} < 2 \ \& \ \Delta R_{\gamma\gamma} < 2$	0.108	-0.675	1.567	0.954	-3.548	2.542
$\sqrt{s} : 14 \text{ TeV}$	$d_1(s)$	$d_2(s)$	$d_3(s)$	$d_4(s)$		
Cuts	$[\lambda_{3H}^2 (g_t^P)^2]$	$[\lambda_{3H} g_t^S (g_t^P)^2]$	$[(g_t^S)^2 (g_t^P)^2]$	$[(g_t^P)^4]$		
No Cuts	0.820	-5.961	13.348	0.707		
$\Delta R_{\gamma\gamma} > 2$	1.561	-10.352	20.409	0.892		
$\Delta R_{\gamma\gamma} < 2$	0.380	-3.266	8.943	0.570		
$\Delta R_{b\bar{b}} > 2$	2.042	-13.668	24.037	1.033		
$\Delta R_{b\bar{b}} < 2$	0.417	-3.081	9.214	0.570		
$\Delta R_{b\bar{b}} > 2 \ \& \ \Delta R_{\gamma\gamma} > 2$	2.402	-12.980	24.976	1.172		
$\Delta R_{b\bar{b}} < 2 \ \& \ \Delta R_{\gamma\gamma} < 2$	0.271	-3.504	7.900	0.541		

TABLE III. The SM cross sections for the process $pp \rightarrow HH \rightarrow \gamma\gamma b\bar{b}$ with various angular-separation cuts on $\Delta R_{bb,\gamma\gamma}$ at the 14 TeV LHC (second column) and at the 100 TeV pp machine (third column). The last column shows them for the process $pp \rightarrow HH \rightarrow \tau^+\tau^- b\bar{b}$ at the 14 TeV LHC. We have taken account of the SM NLO cross section $\sigma_{\text{SM}}(pp \rightarrow HH) \simeq 34$ fb, the Higgs branching fractions, and both the photon and b -quark reconstruction efficiencies. The p_T dependence of b -tagging efficiency is considered and 0.5 is taken for the τ -tagging efficiency. Also considered is the mis-tagging probability of $P_{j \rightarrow \tau} = 0.01$. Results are at the detector level using the ATLAS template in Delphes v.3.

Cuts Cross Section (fb)	SM-14 ($\gamma\gamma b\bar{b}$)	SM-100 ($\gamma\gamma b\bar{b}$)	SM-14 ($\tau^+\tau^- b\bar{b}$)
$\Delta R_{\gamma\gamma/\tau^+\tau^-} > 2$	1.80×10^{-2}	6.86×10^{-1}	5.12×10^{-2}
$\Delta R_{\gamma\gamma/\tau^+\tau^-} < 2$	4.60×10^{-2}	1.84	9.20×10^{-2}
$\Delta R_{bb} > 2$	2.00×10^{-3}	6.46×10^{-2}	5.50×10^{-2}
$\Delta R_{bb} < 2$	9.99×10^{-3}	3.42×10^{-1}	2.70×10^{-1}
$\Delta R_{bb} > 2$ & $\Delta R_{\gamma\gamma/\tau^+\tau^-} > 2$	7.20×10^{-4}	1.79×10^{-2}	1.17×10^{-3}
$\Delta R_{bb} < 2$ & $\Delta R_{\gamma\gamma/\tau^+\tau^-} < 2$	5.89×10^{-3}	2.05×10^{-1}	1.03×10^{-2}

TABLE IV. **100 TeV pp machine:** The coefficients for the ratio of the cross sections $\sigma(gg \rightarrow HH)/\sigma_{\text{SM}}(gg \rightarrow HH)$ as in Eq. (7) with and without the angular-separation cuts of $\Delta R_{\gamma\gamma} >$ or < 2 ; $\Delta R_{b\bar{b}} >$ or < 2 ; and $\Delta R_{\gamma\gamma}$ and $\Delta R_{b\bar{b}}$ both > 2 or < 2 . The relevant coefficients for the **CPC1** scenario are c_1, c_2, c_3 ; those for the **CPC2** scenario are $c_1, c_2, c_3, e_1, e_2, e_3$; and those for the **CPV1** scenario are $c_1, c_2, c_3, d_1, d_2, d_3, d_4$. Results are at the detector level using the ATLAS template in Delphes v.3.

$\sqrt{s} : 100 \text{ TeV}$	$c_1(s)$	$c_2(s)$	$c_3(s)$	$e_1(s)$	$e_2(s)$	$e_3(s)$
Cuts	$[\lambda_{3H}^2 (g_t^S)^2]$	$[\lambda_{3H} (g_t^S)^3]$	$[(g_t^S)^4]$	$[\lambda_{3H} g_t^S g_{tt}^S]$	$[g_{tt}^S (g_t^S)^2]$	$[(g_{tt}^S)^2]$
No Cuts	0.208	-1.108	1.900	1.214	-4.137	2.974
$\Delta R_{\gamma\gamma} > 2$	0.384	-1.619	2.235	1.437	-4.183	2.126
$\Delta R_{\gamma\gamma} < 2$	0.119	-0.859	1.740	1.085	-4.080	3.281
$\Delta R_{b\bar{b}} > 2$	0.479	-2.070	2.592	2.620	-5.302	3.026
$\Delta R_{b\bar{b}} < 2$	0.126	-0.769	1.643	1.624	-4.285	3.519
$\Delta R_{b\bar{b}} > 2$ & $\Delta R_{\gamma\gamma} > 2$	0.607	-2.536	2.929	2.553	-5.920	3.160
$\Delta R_{b\bar{b}} < 2$ & $\Delta R_{\gamma\gamma} < 2$	0.099	-0.680	1.581	1.592	-4.059	3.468
$\sqrt{s} : 100\text{TeV}$	$d_1(s)$	$d_2(s)$	$d_3(s)$	$d_4(s)$		
Cuts	$[\lambda_{3H}^2 (g_t^P)^2]$	$[\lambda_{3H} g_t^S (g_t^P)^2]$	$[(g_t^S)^2 (g_t^P)^2]$	$[(g_t^P)^4]$		
No Cuts	0.635	-4.789	11.225	0.683		
$\Delta R_{\gamma\gamma} > 2$	1.209	-7.687	13.519	0.728		
$\Delta R_{\gamma\gamma} < 2$	0.336	-3.367	9.955	0.642		
$\Delta R_{b\bar{b}} > 2$	1.883	-11.795	20.282	1.062		
$\Delta R_{b\bar{b}} < 2$	0.422	-3.804	11.404	0.706		
$\Delta R_{b\bar{b}} > 2$ & $\Delta R_{\gamma\gamma} > 2$	2.434	-14.111	20.250	1.494		
$\Delta R_{b\bar{b}} < 2$ & $\Delta R_{\gamma\gamma} < 2$	0.284	-3.286	10.148	0.685		

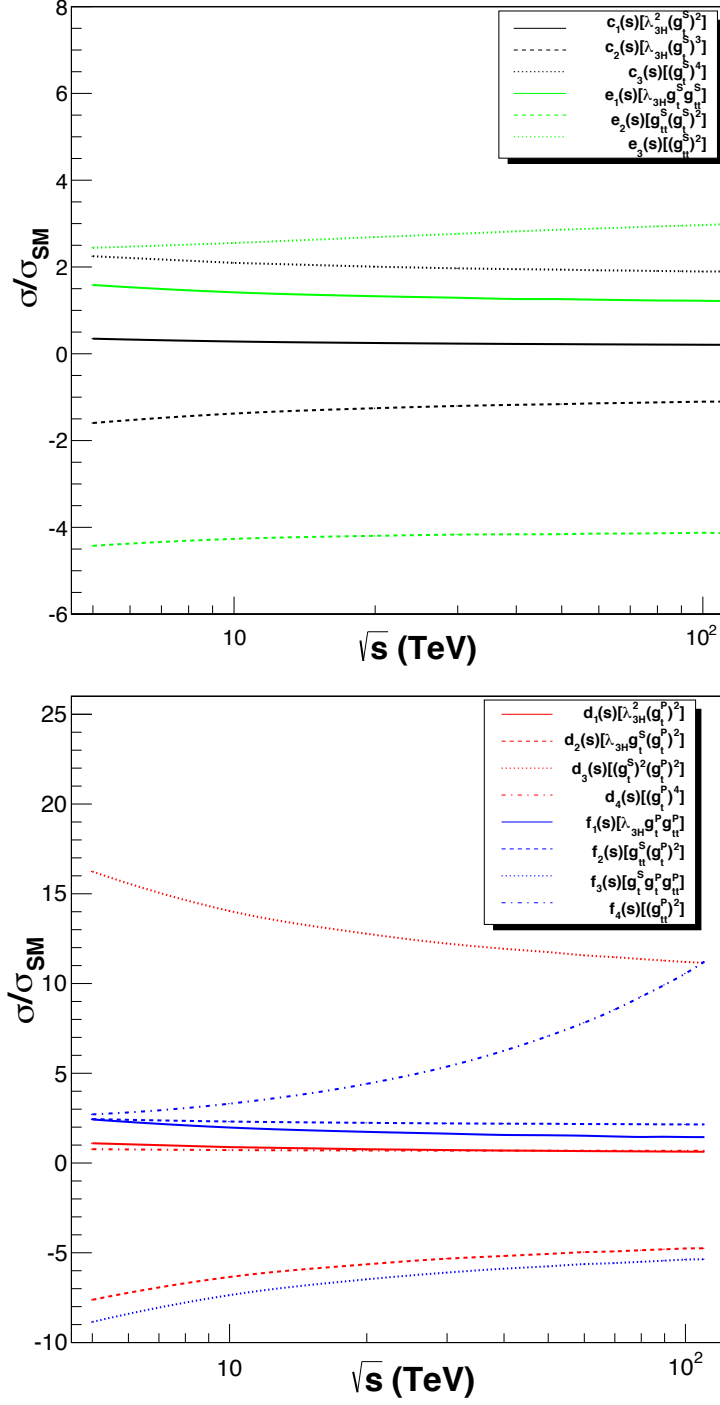


FIG. 1. The coefficients $c_i(s)$ and $e_i(s)$ (upper) with $i = 1, 2, 3$ and $d_j(s)$ and $f_j(s)$ (lower) with $j = 1, 2, 3, 4$ as functions of s .

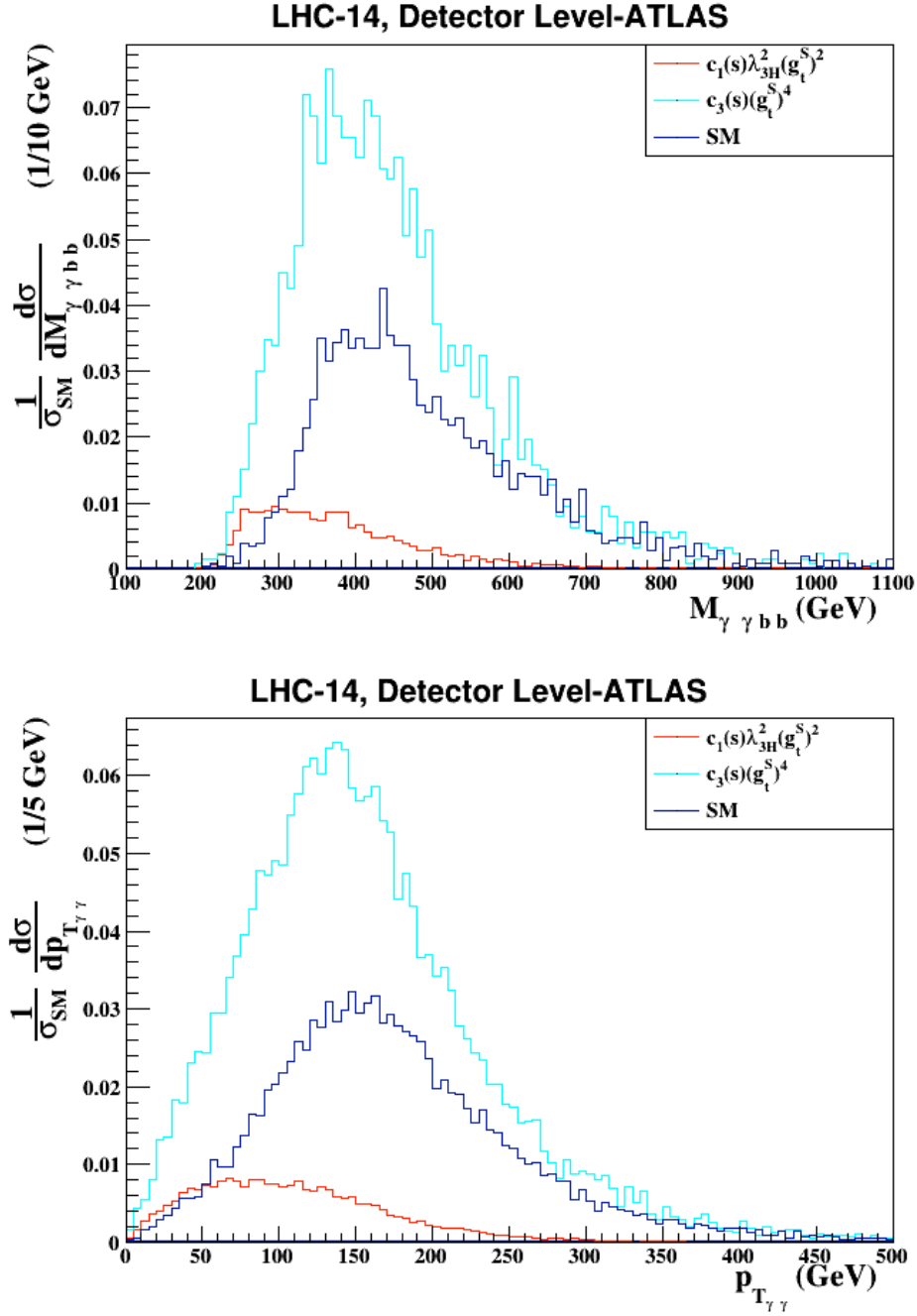


FIG. 2. CPC1: Distributions in $M_{\gamma\gamma b\bar{b}}$ (upper) and $p_{T,\gamma\gamma}$ (lower) in the decay products of the Higgs boson pair with detector simulation.

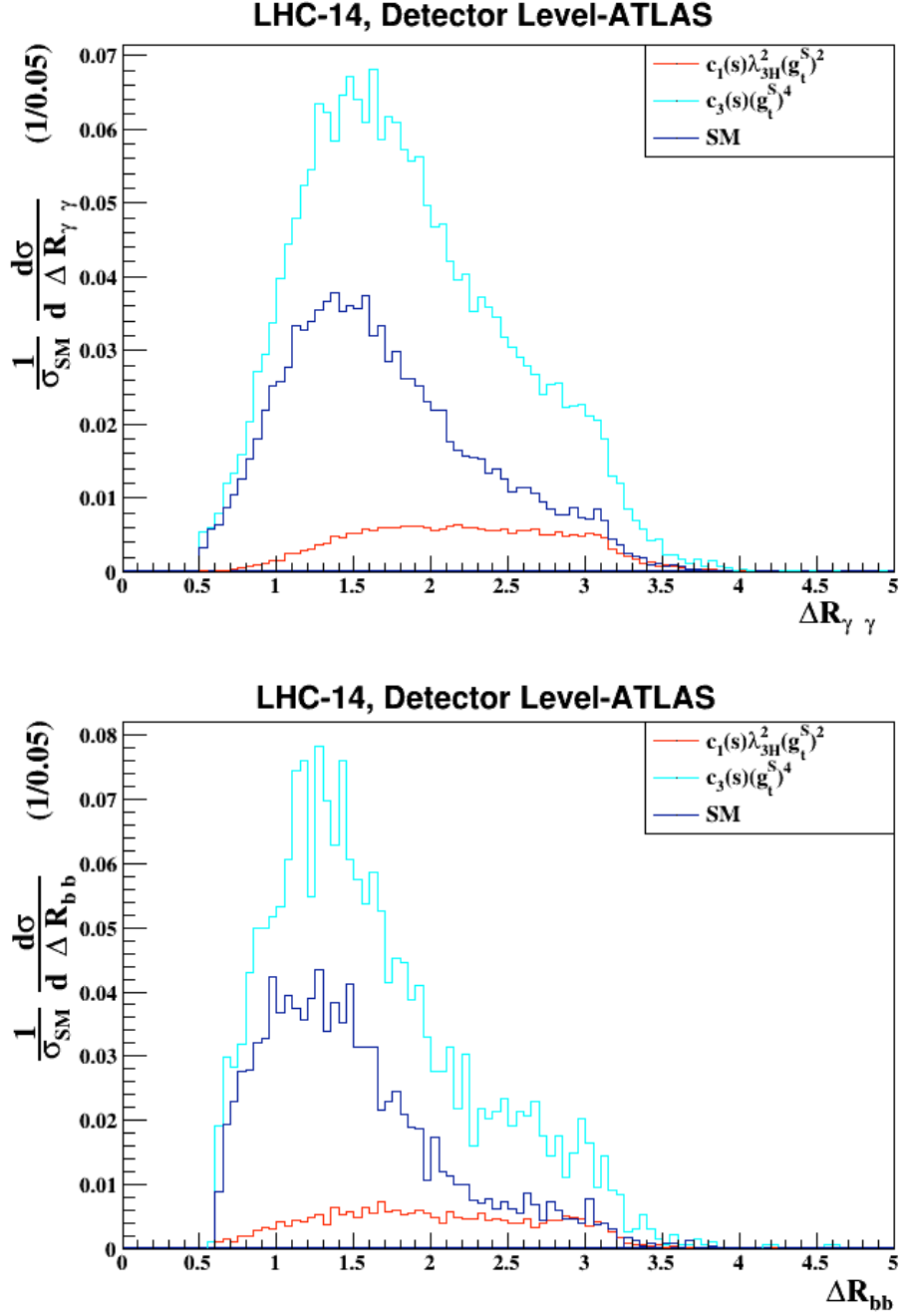


FIG. 3. **CPC1**: Distributions in $\Delta R_{\gamma\gamma}$ (upper) and $\Delta R_{b\bar{b}}$ (lower) in the decay products of the Higgs boson pair with detector simulation.

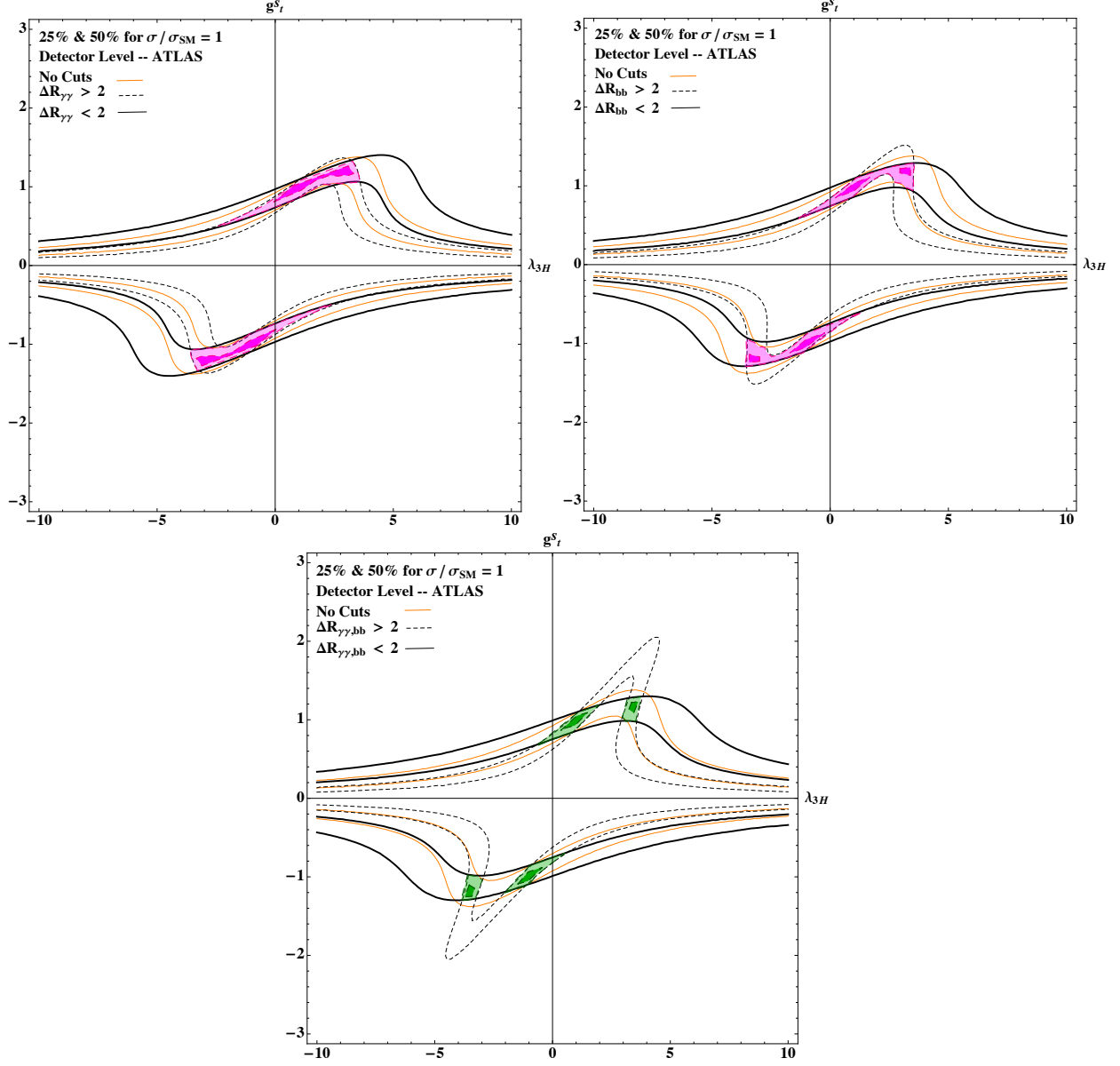


FIG. 4. **CPC1**: The 25% and 50% sensitivity regions bounded by three measurements of cross sections with no cuts, $\Delta R_{\gamma\gamma} > 2$, and $\Delta R_{\gamma\gamma} < 2$ (the upper-left panel); with no cuts, $\Delta R_{b\bar{b}} > 2$, and $\Delta R_{b\bar{b}} < 2$ (the upper-right panel); and no cuts, $\Delta R_{\gamma\gamma}$, $\Delta R_{b\bar{b}} > 2$, and $\Delta R_{\gamma\gamma}$, $\Delta R_{b\bar{b}} < 2$ (the lower panel). We assume that the measurements agree with the SM values with uncertainties of 25% and 50%, respectively.

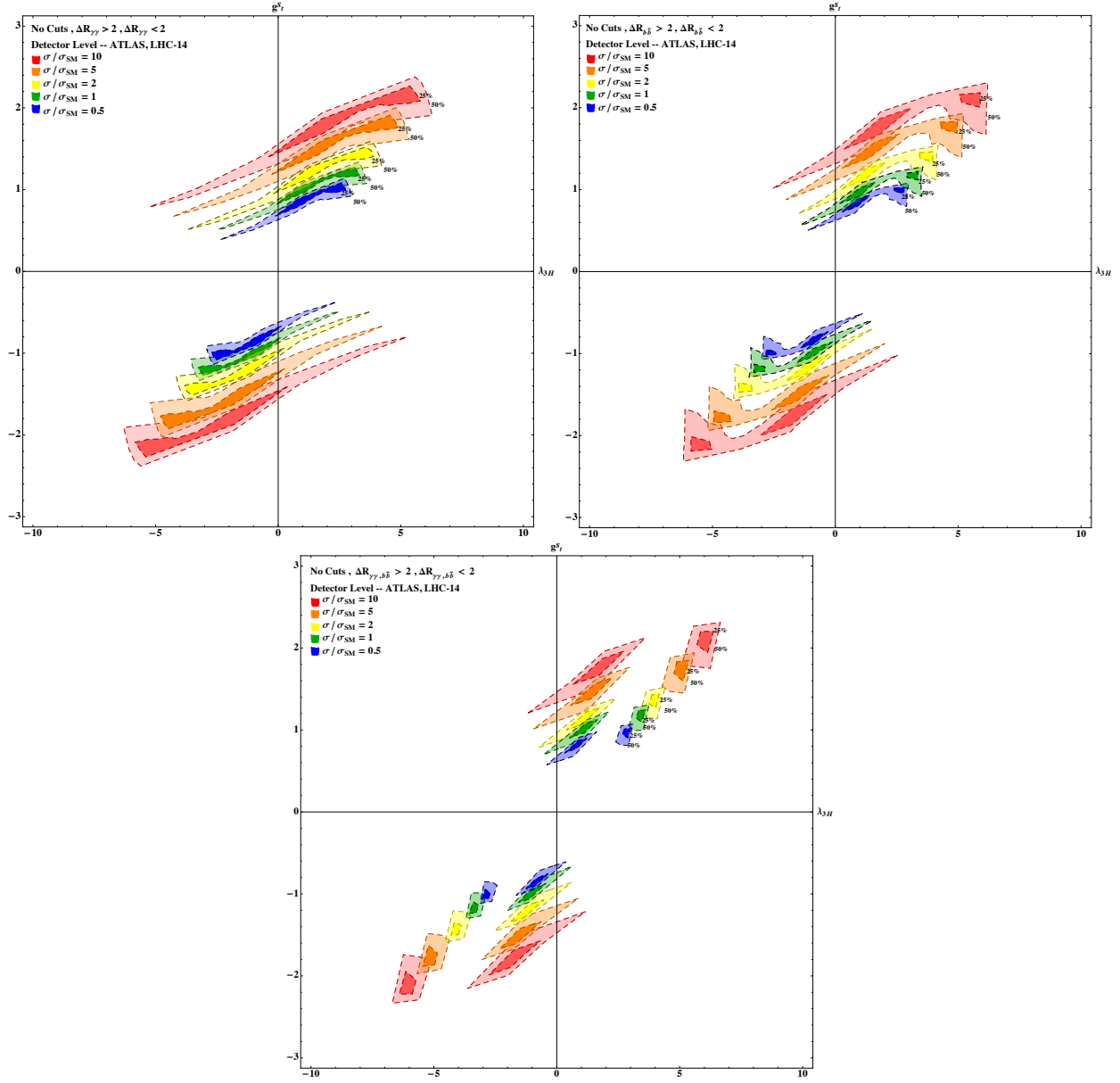


FIG. 5. **CPC1**: The same as Fig. 4 but we assume $\sigma/\sigma_{\text{SM}} = 0.5 - 10$.

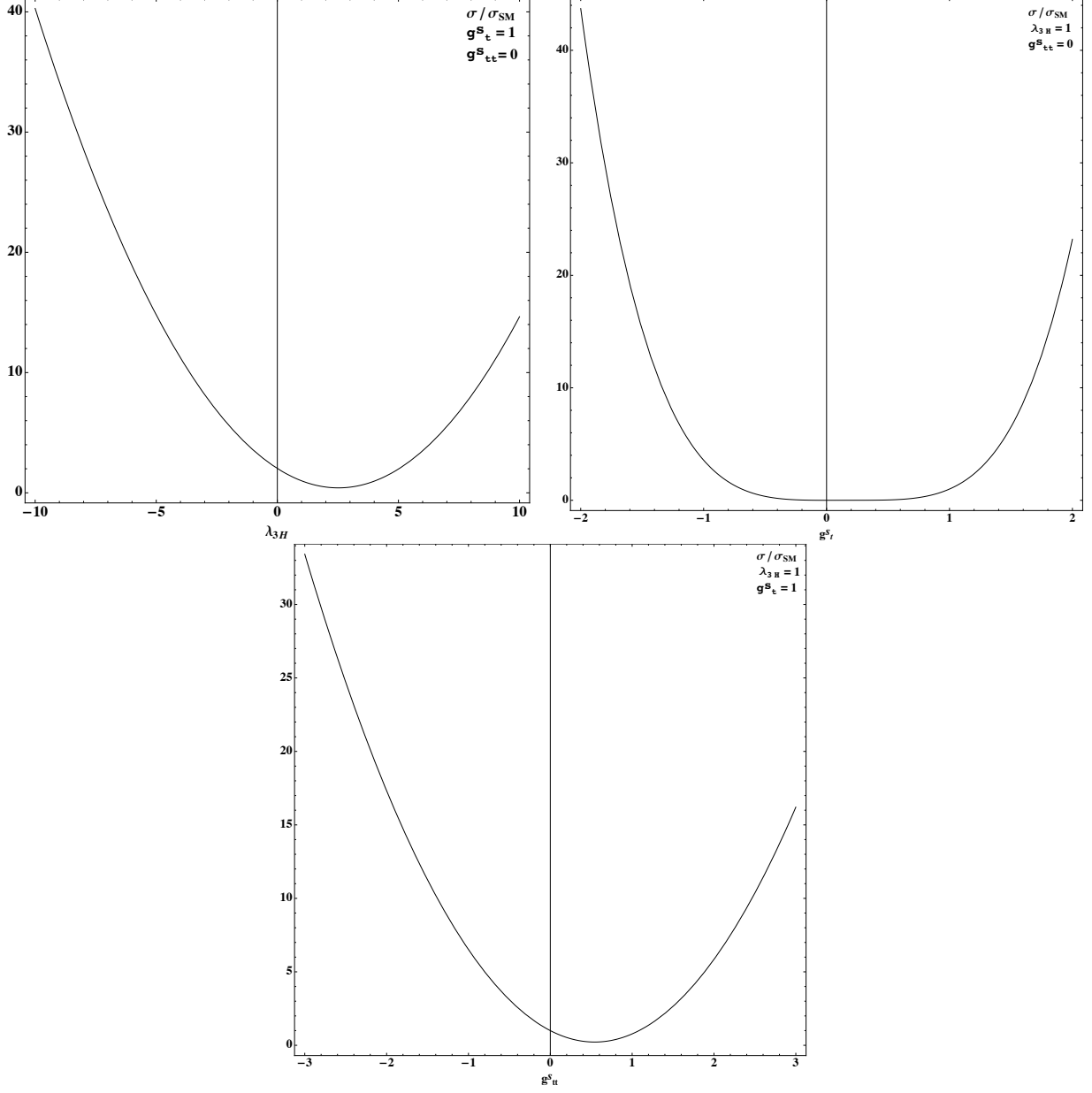


FIG. 6. **CPC2**: Variation of the ratio $\sigma/\sigma_{\text{SM}}$ using Eq. (7) versus λ_{3H} (upper-left), g_t^S (upper-right), and g_{tt}^S (lower) while keeping the other two parameters at their corresponding SM values.

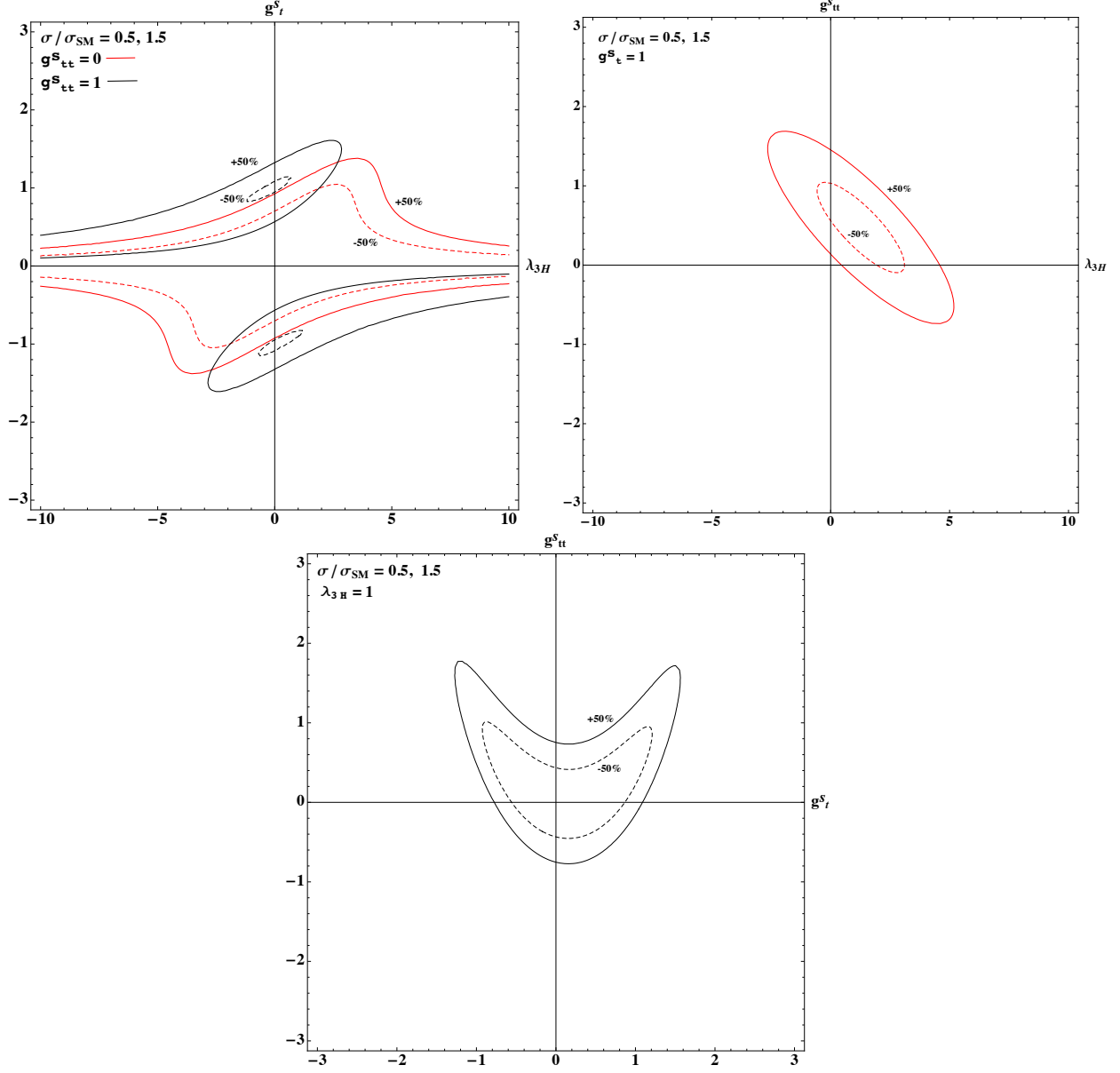


FIG. 7. **CPC2:** Contours marked by $\sigma/\sigma_{\text{SM}} = 0.5, 1.5$ for (λ_{3H}, g_t^S) (upper-left), (λ_{3H}, g_{tt}^S) (upper-right), and (g_t^S, g_{tt}^S) (lower).

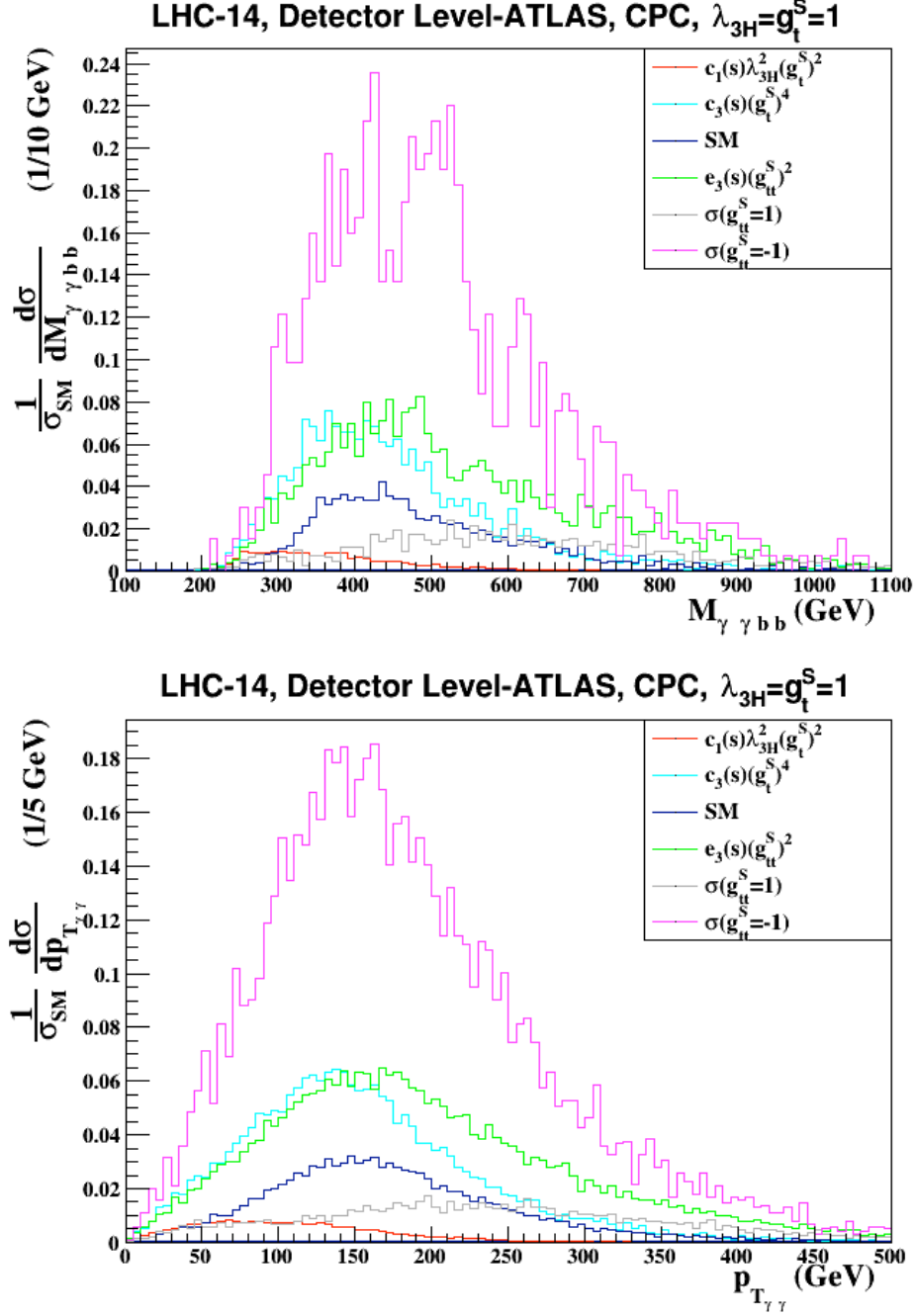


FIG. 8. CPC2: Distributions in $M_{\gamma\gamma b\bar{b}}$ (upper) and $p_{T\gamma\gamma}$ (lower) in the decay products of the Higgs boson pair with detector simulation.

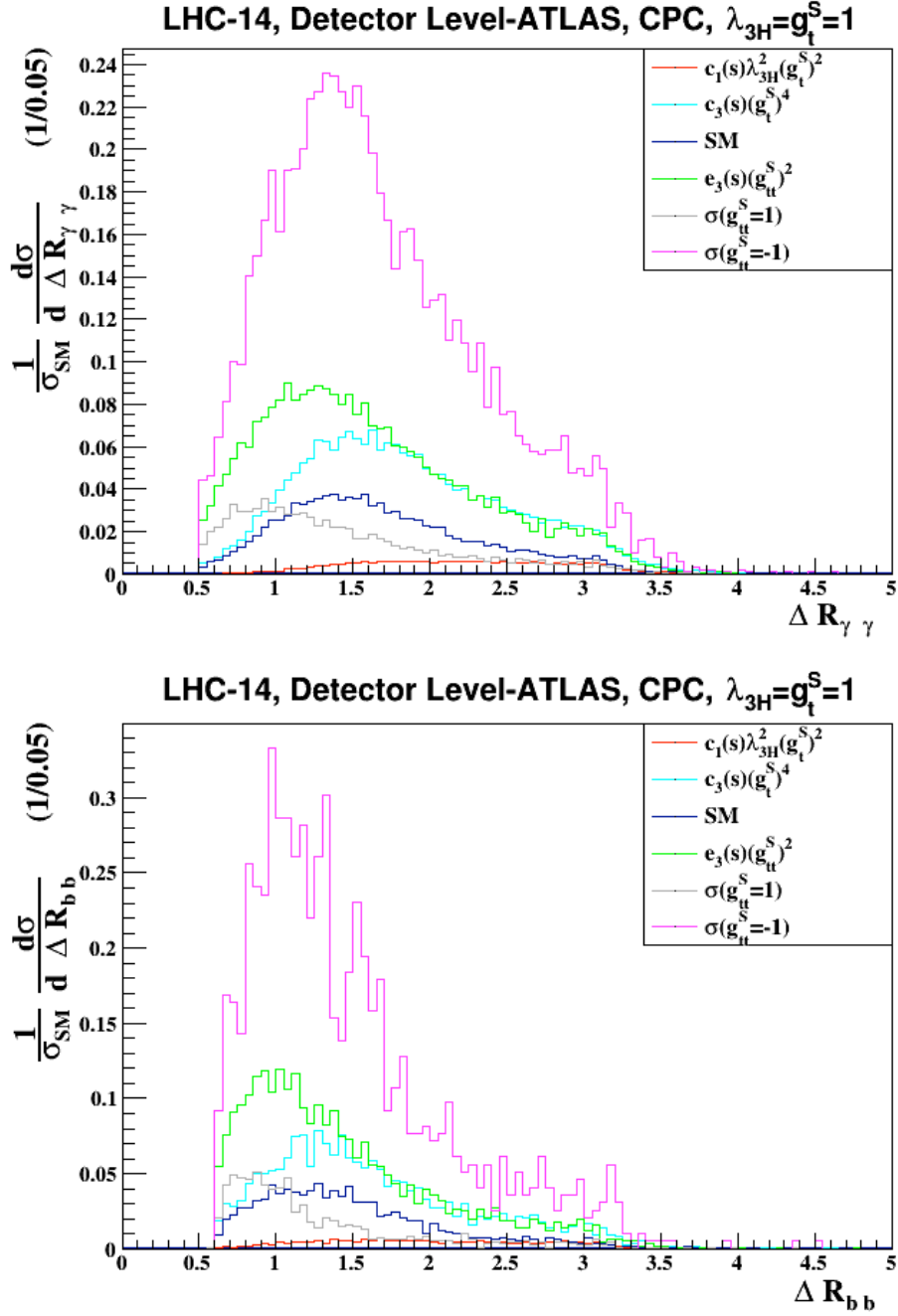


FIG. 9. **CPC2**: Angular distributions of $\Delta R_{\gamma\gamma}$ and $\Delta R_{b\bar{b}}$ between the two photons and between the two b quarks.

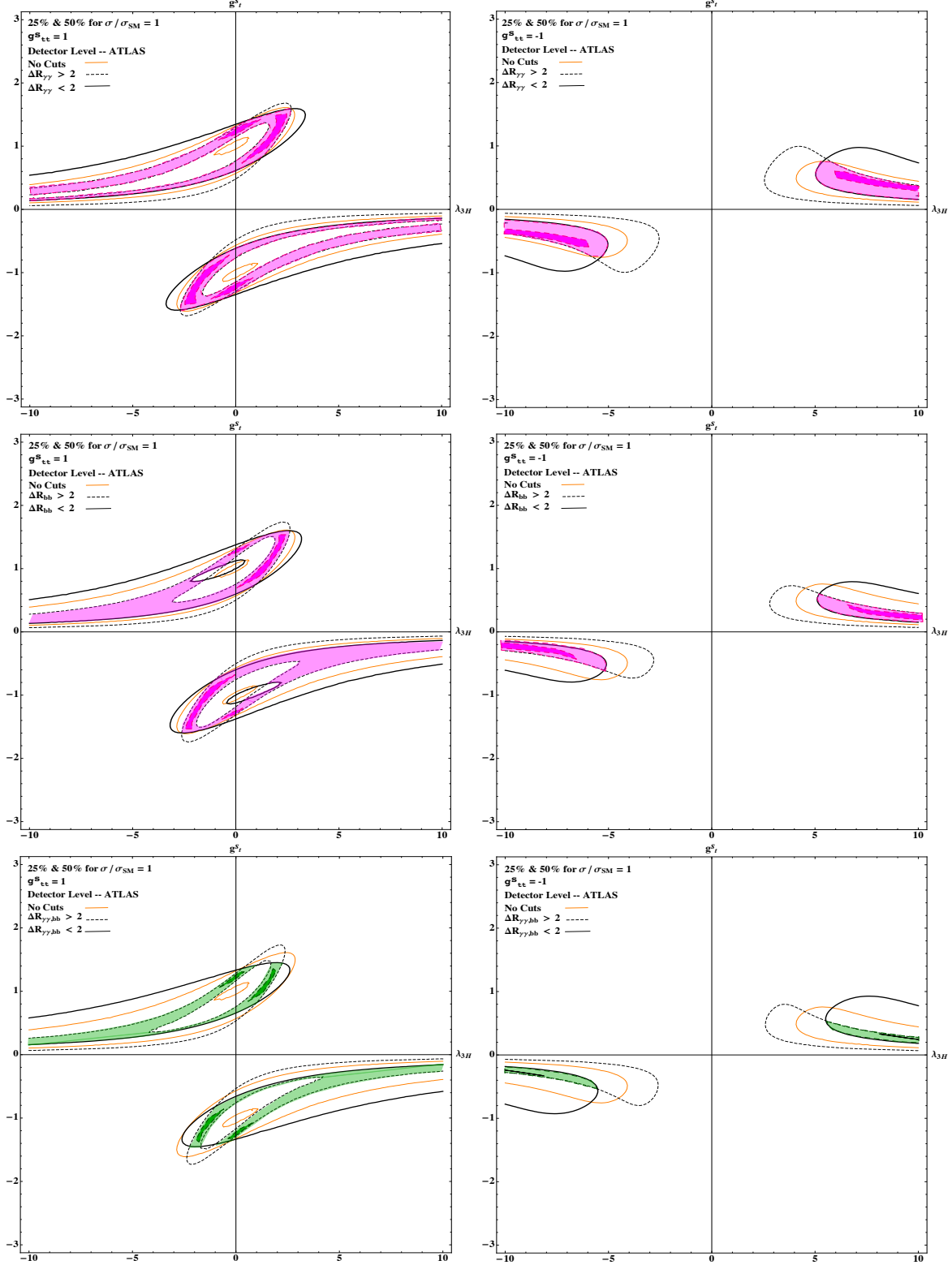


FIG. 10. **CPC2**: The 25% and 50% sensitivity regions in (λ_{3H}, g_t^S) bounded by three measurements of cross sections with no cuts, $\Delta R_{\gamma\gamma} > 2$, and $\Delta R_{\gamma\gamma} < 2$ (the upper panels); with no cuts, $\Delta R_{b\bar{b}} > 2$, and $\Delta R_{b\bar{b}} < 2$ (the middle panels); and no cuts, $\Delta R_{\gamma\gamma}$, $\Delta R_{b\bar{b}} > 2$, and $\Delta R_{\gamma\gamma}$, $\Delta R_{b\bar{b}} < 2$ (the lower panels). The left panels are for $g_{tt}^S = 1$ while those on the right are for $g_{tt}^S = -1$. We assume that the measurements agree with the SM values with uncertainties of 25% and 50%, respectively.

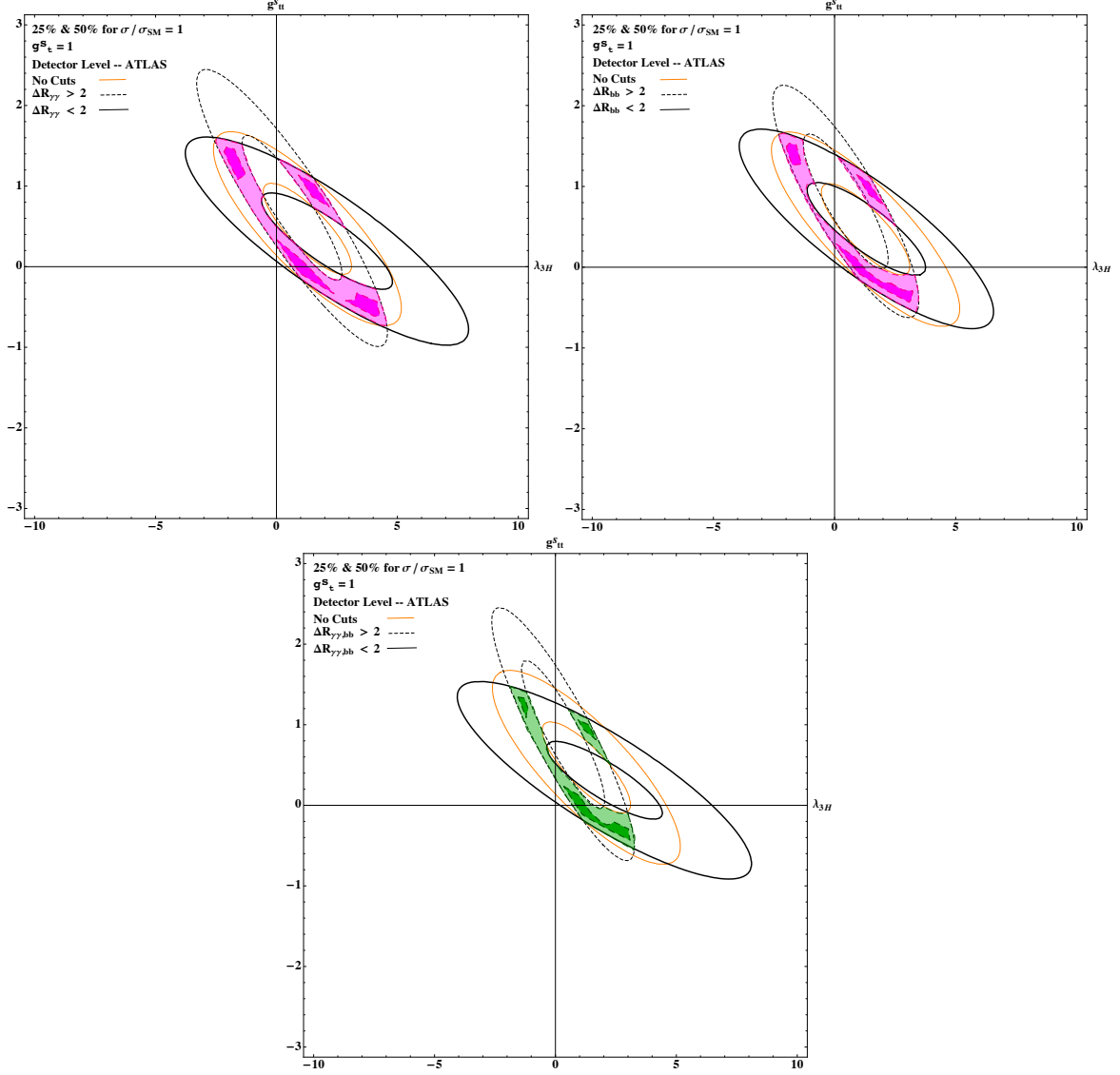


FIG. 11. **CPC2**: similar to Fig. 10 but in the plane of (λ_{3H}, g_{tt}^S) .

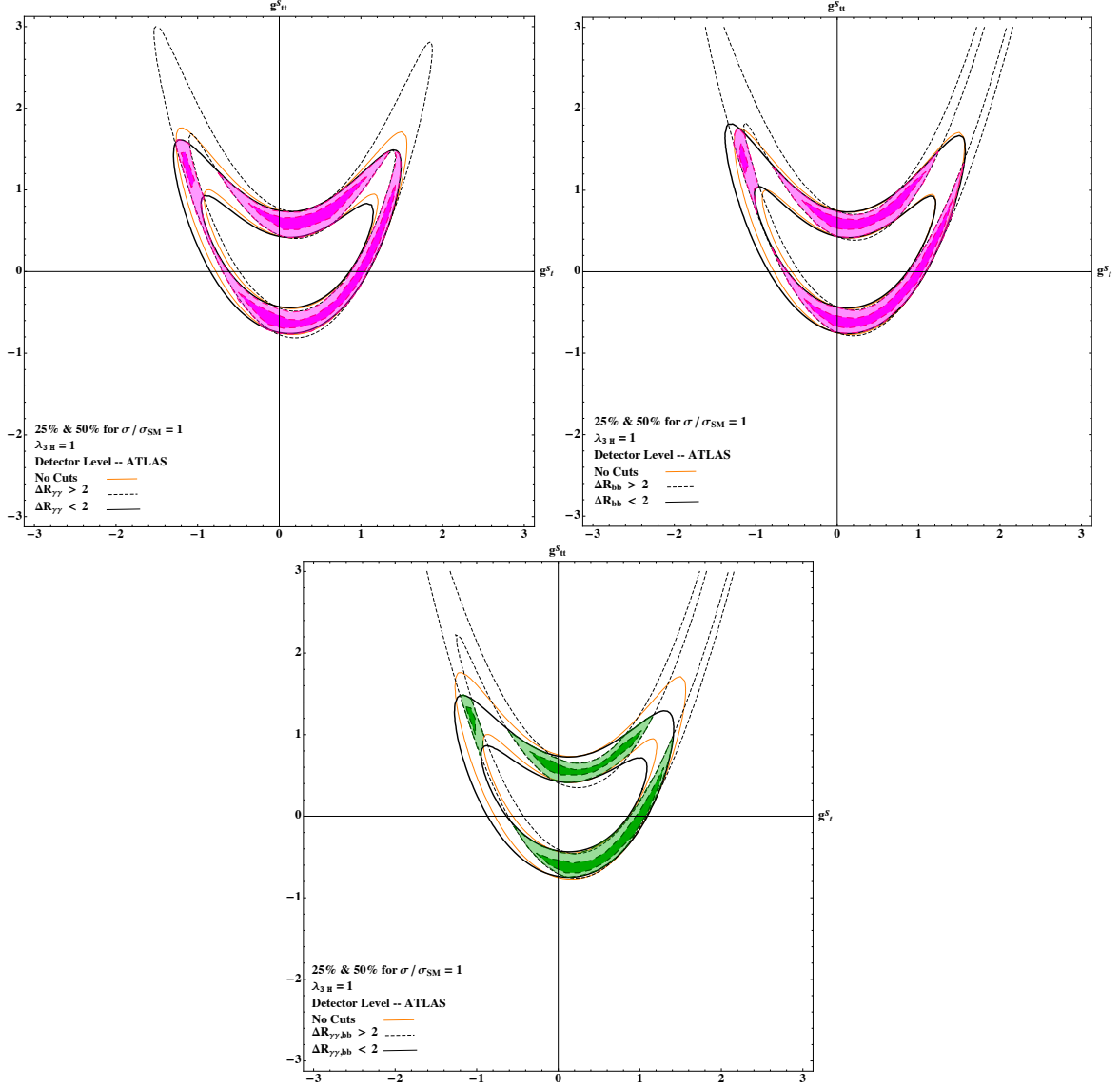


FIG. 12. **CPC2**: similar to Fig. 10 but in the plane of (g_t^S, g_{tt}^S) .

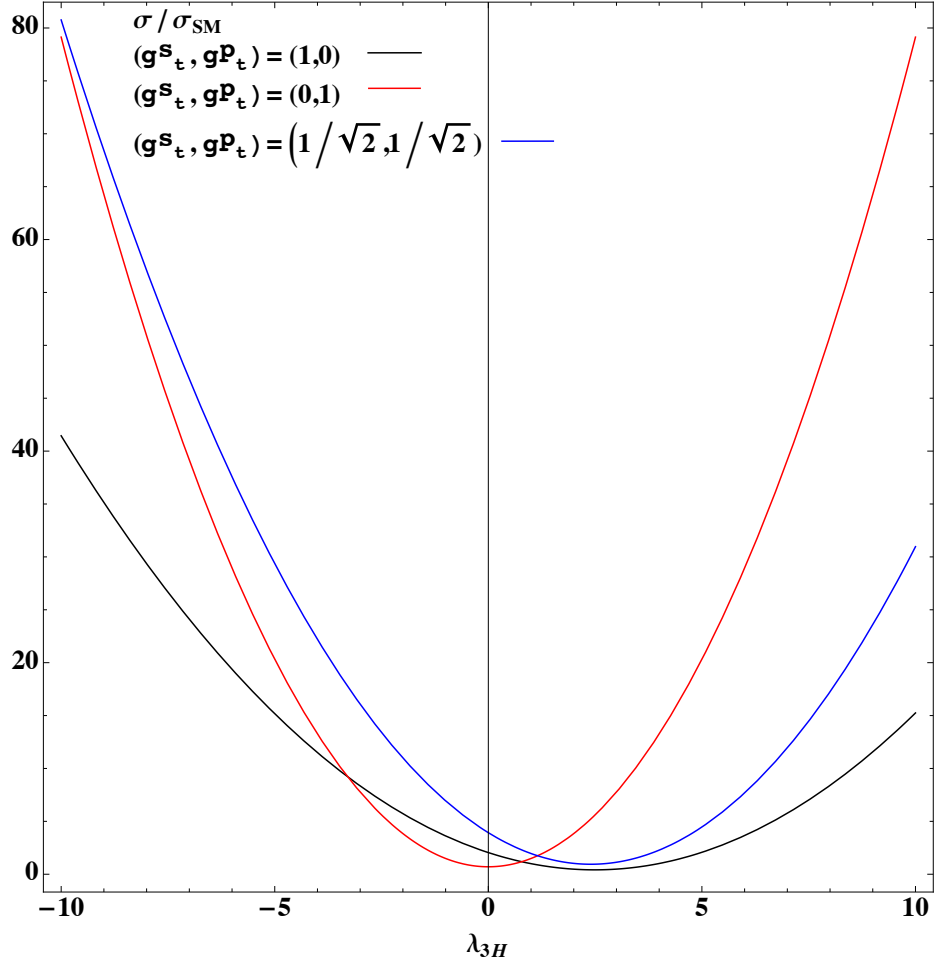


FIG. 13. **CPV1:** The ratio $\sigma/\sigma_{\text{SM}}$ versus λ_{3H} for $(g_t^S, g_t^P) = (1, 0), (0, 1), (1/\sqrt{2}, 1/\sqrt{2})$

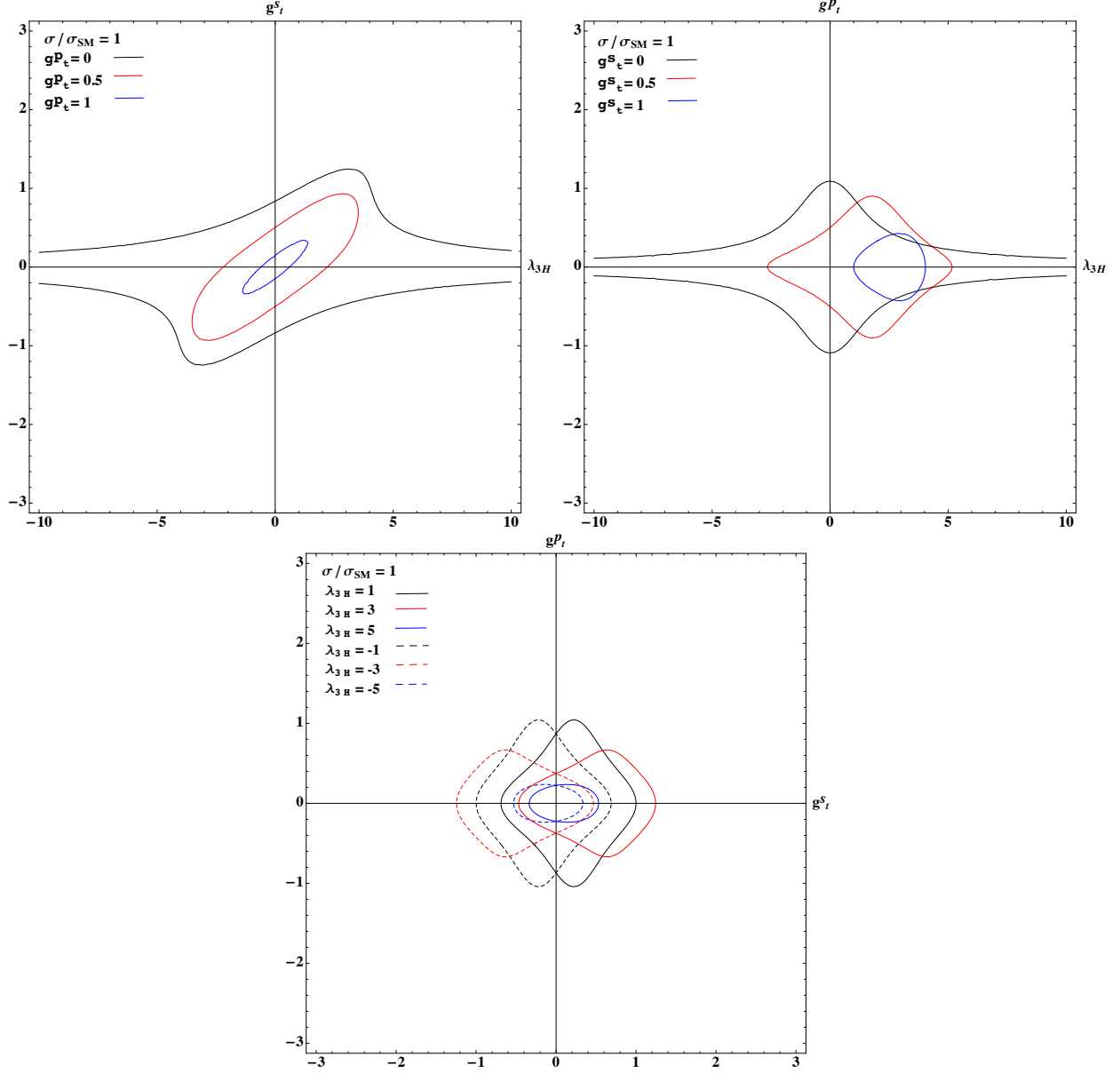


FIG. 14. **CPV1:** Contours for the ratio $\sigma/\sigma_{\text{SM}} = 1$ in the plane of (λ_{3H}, g_t^S) (upper-left), (λ_{3H}, g_t^P) (upper-right), and (g_t^S, g_t^P) (lower) for a few values of the third parameter.

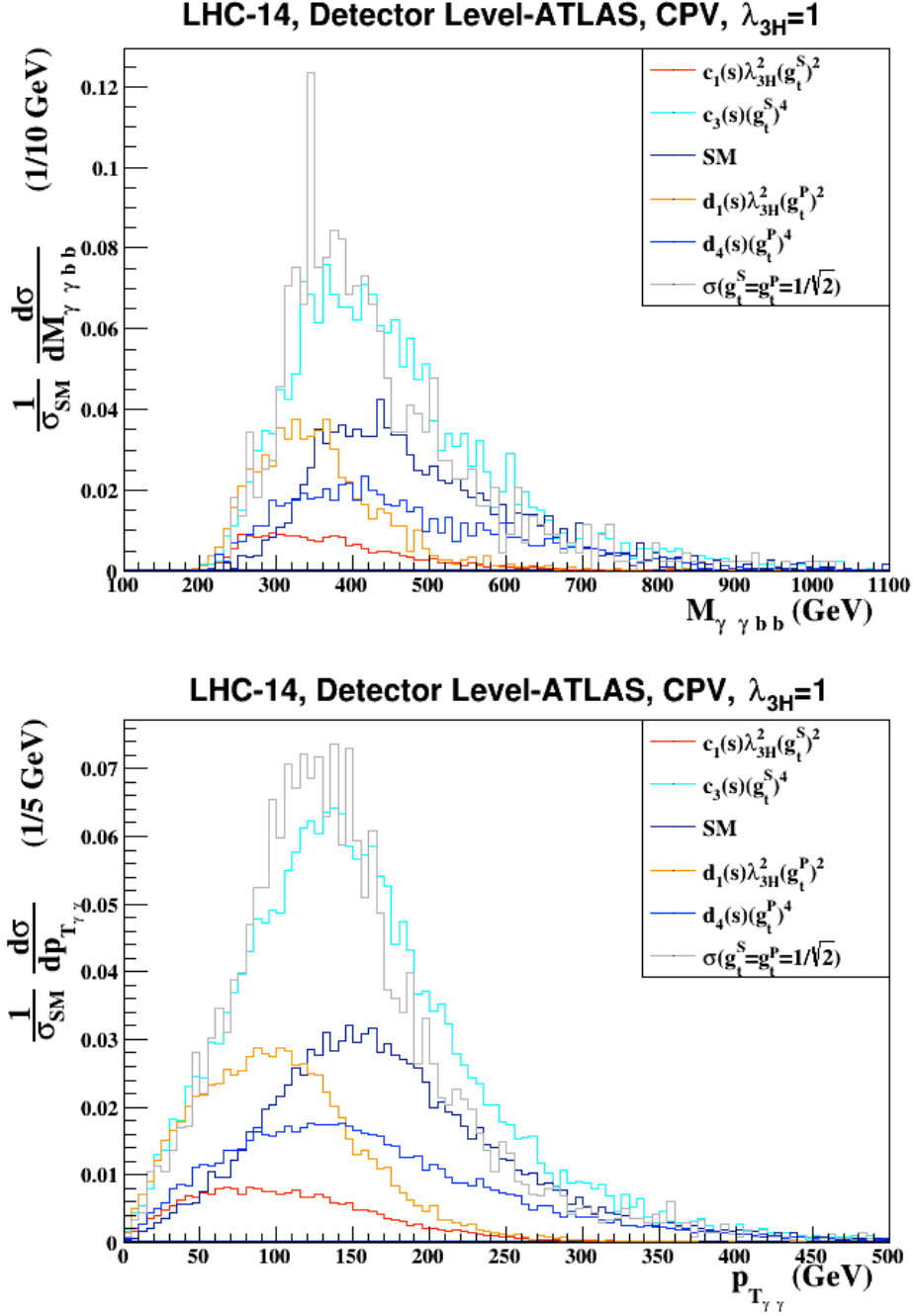


FIG. 15. **CPV1**: Invariant mass distribution $M_{\gamma\gamma b\bar{b}}$ and $p_{T,\gamma\gamma}$ for the decay products of the Higgs-boson pair.

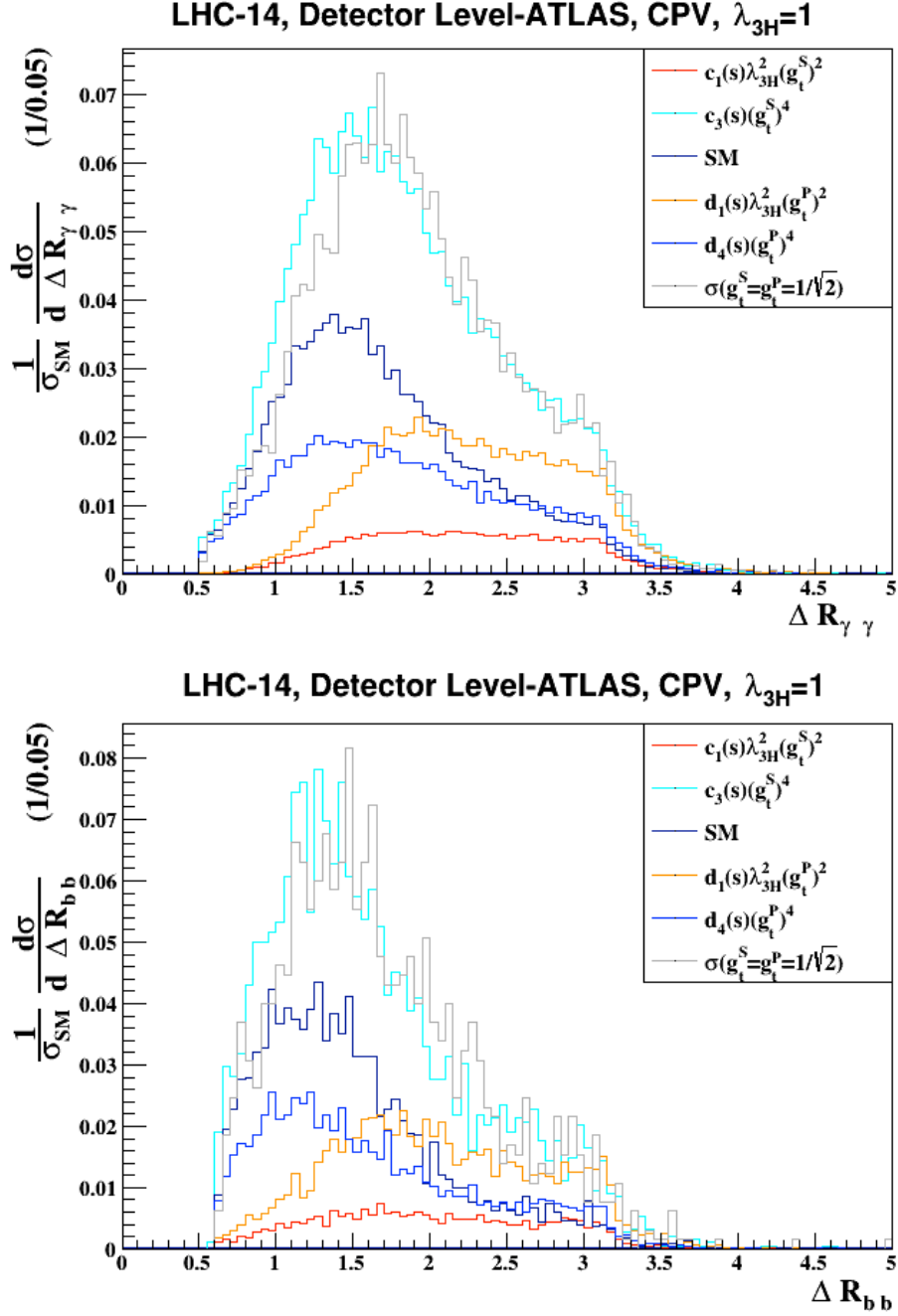


FIG. 16. CPV1: Angular distributions of $\Delta R_{\gamma\gamma}$ and $\Delta R_{b\bar{b}}$ between the two photons and between the two b quarks

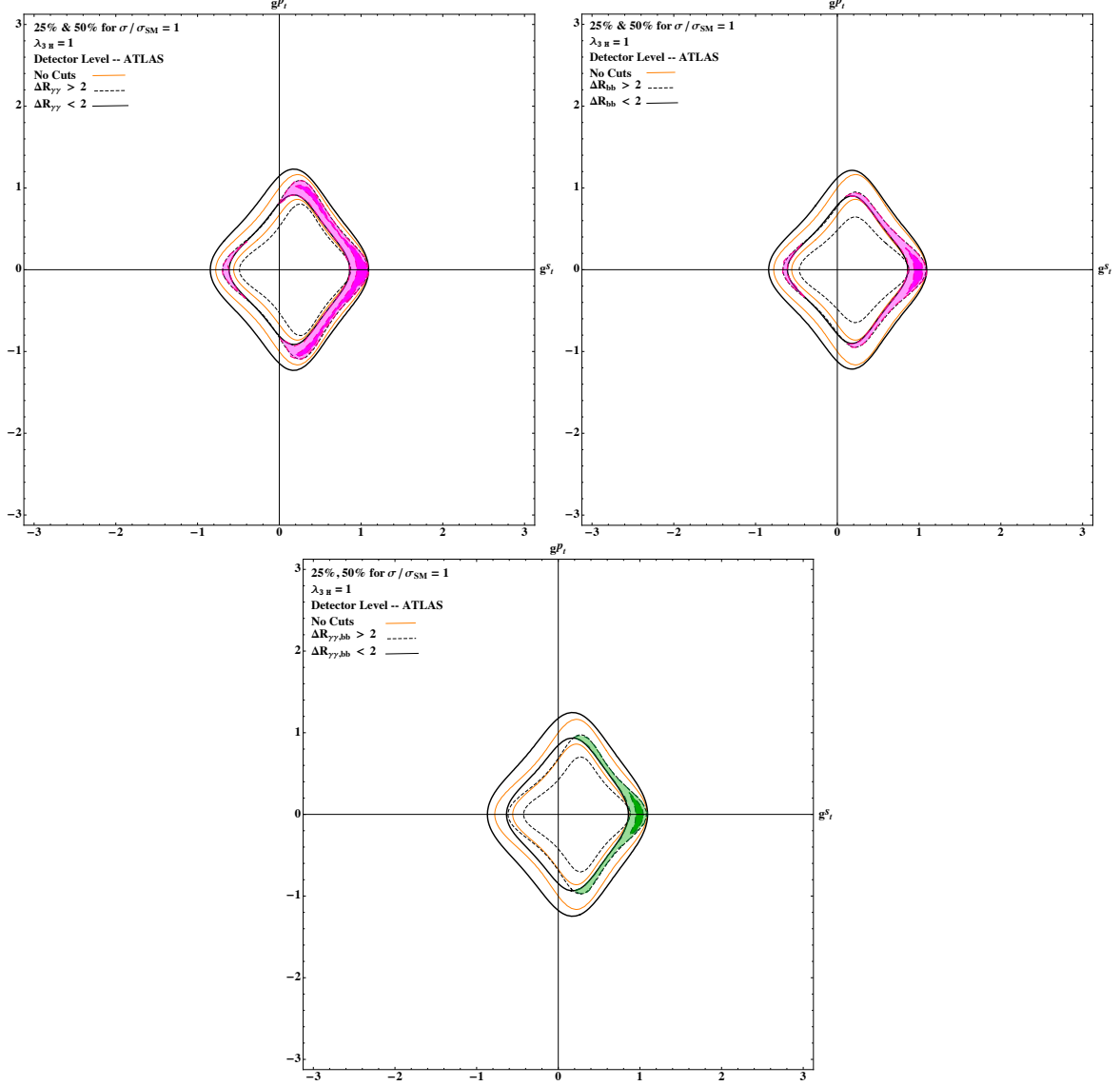


FIG. 17. **CPV1**: The 25% and 50% sensitivity regions in the plane (g_t^S, g_t^P) bounded by three measurements of cross sections with no cuts, $\Delta R_{\gamma\gamma} > 2$, and $\Delta R_{\gamma\gamma} < 2$ (the upper-left panel); with no cuts, $\Delta R_{b\bar{b}} > 2$, and $\Delta R_{b\bar{b}} < 2$ (the upper-right panel); and no cuts, $\Delta R_{\gamma\gamma}$, $\Delta R_{b\bar{b}} > 2$, and $\Delta R_{\gamma\gamma}$, $\Delta R_{b\bar{b}} < 2$ (the lower panel). We assume that the measurements agree with the SM values with uncertainties of 25% and 50%, respectively.

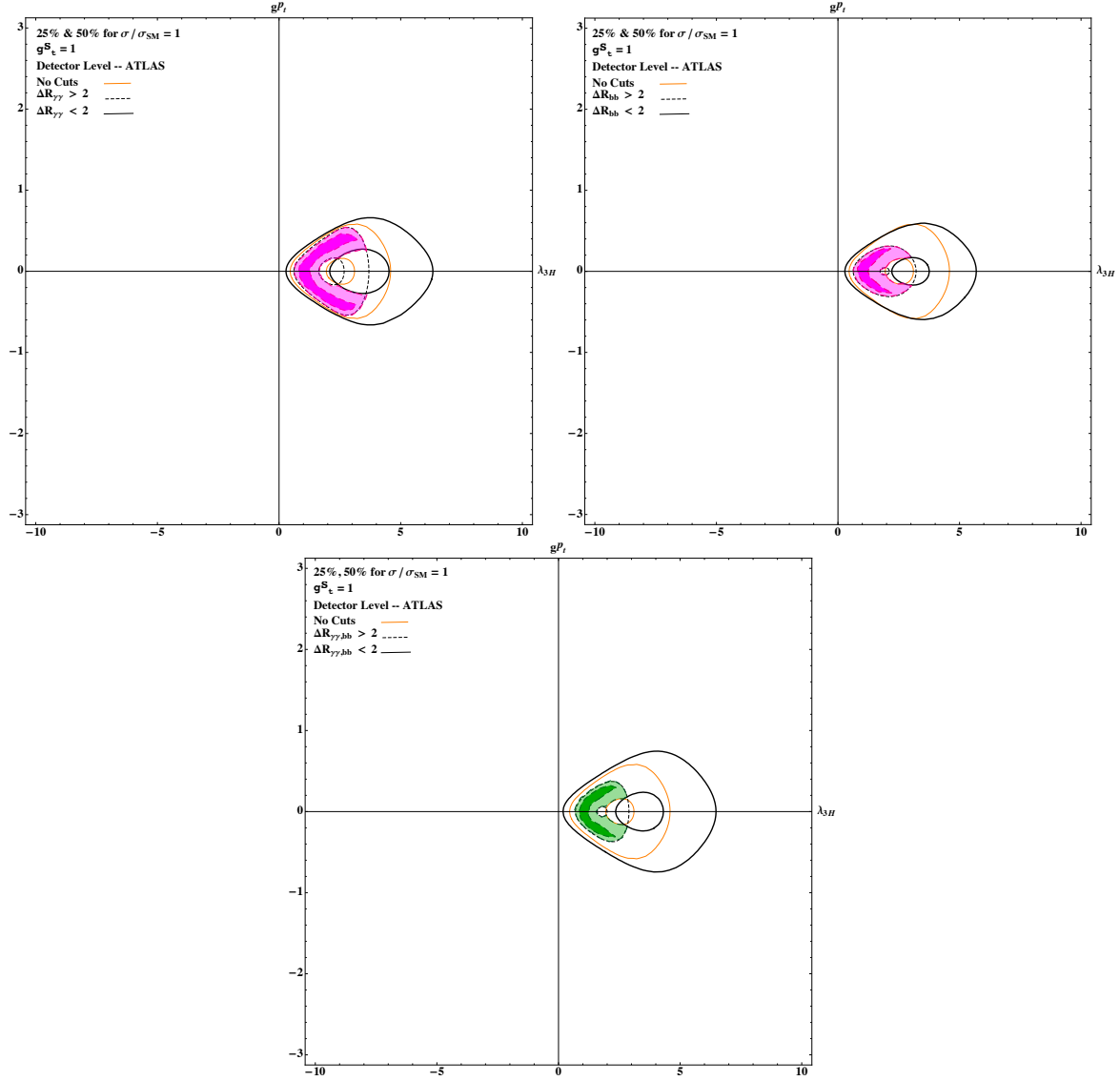


FIG. 18. **CPV1**: similar to Fig. 17 but in the plane of (λ_{3H}, g_t^P) .

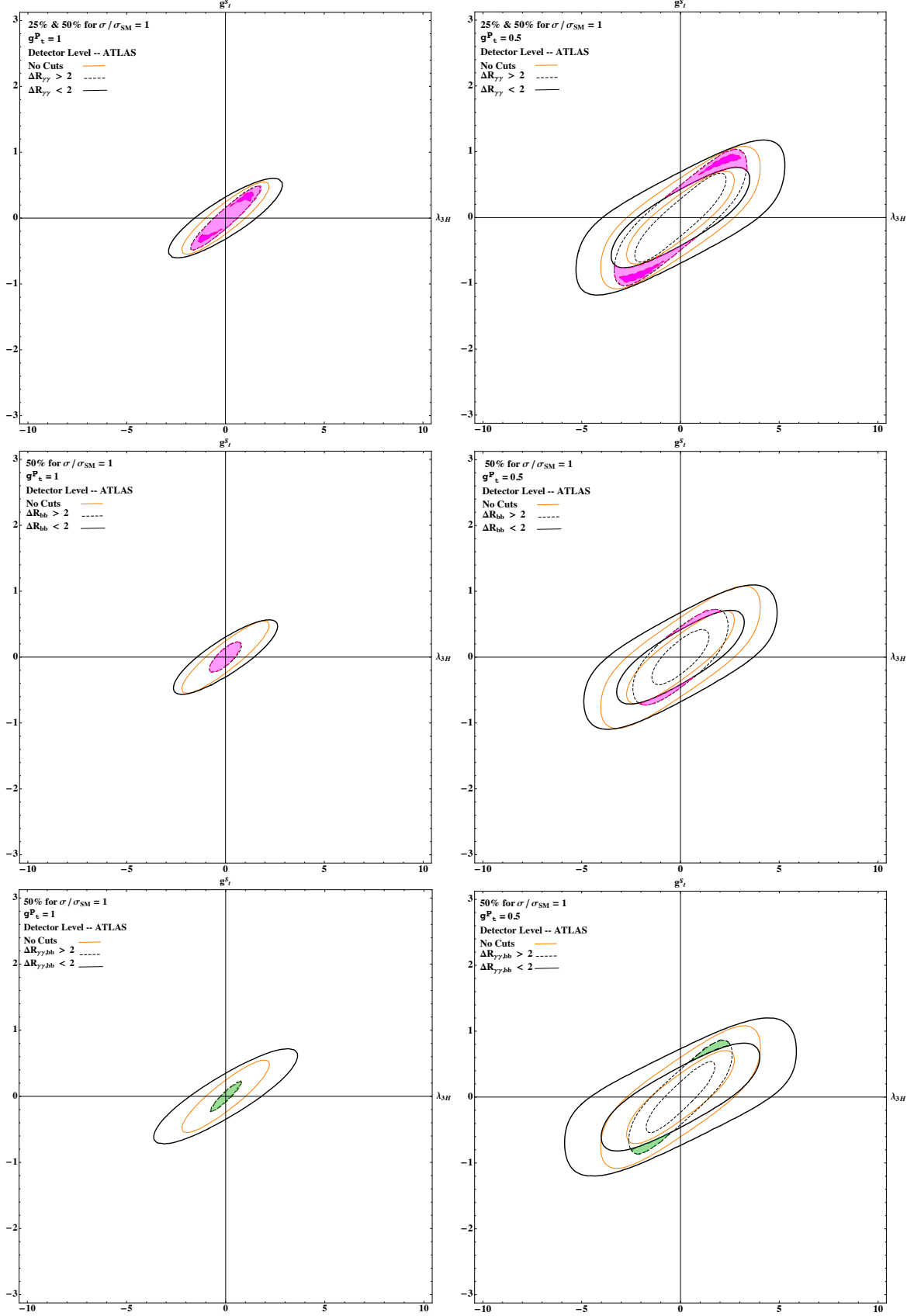


FIG. 19. **CPV1**: similar to Fig. 17 but in the plane of (λ_{3H}, g_t^S) . The left panels are for $g_t^P = 1$ while those on the right are for $g_t^P = 0.5$.

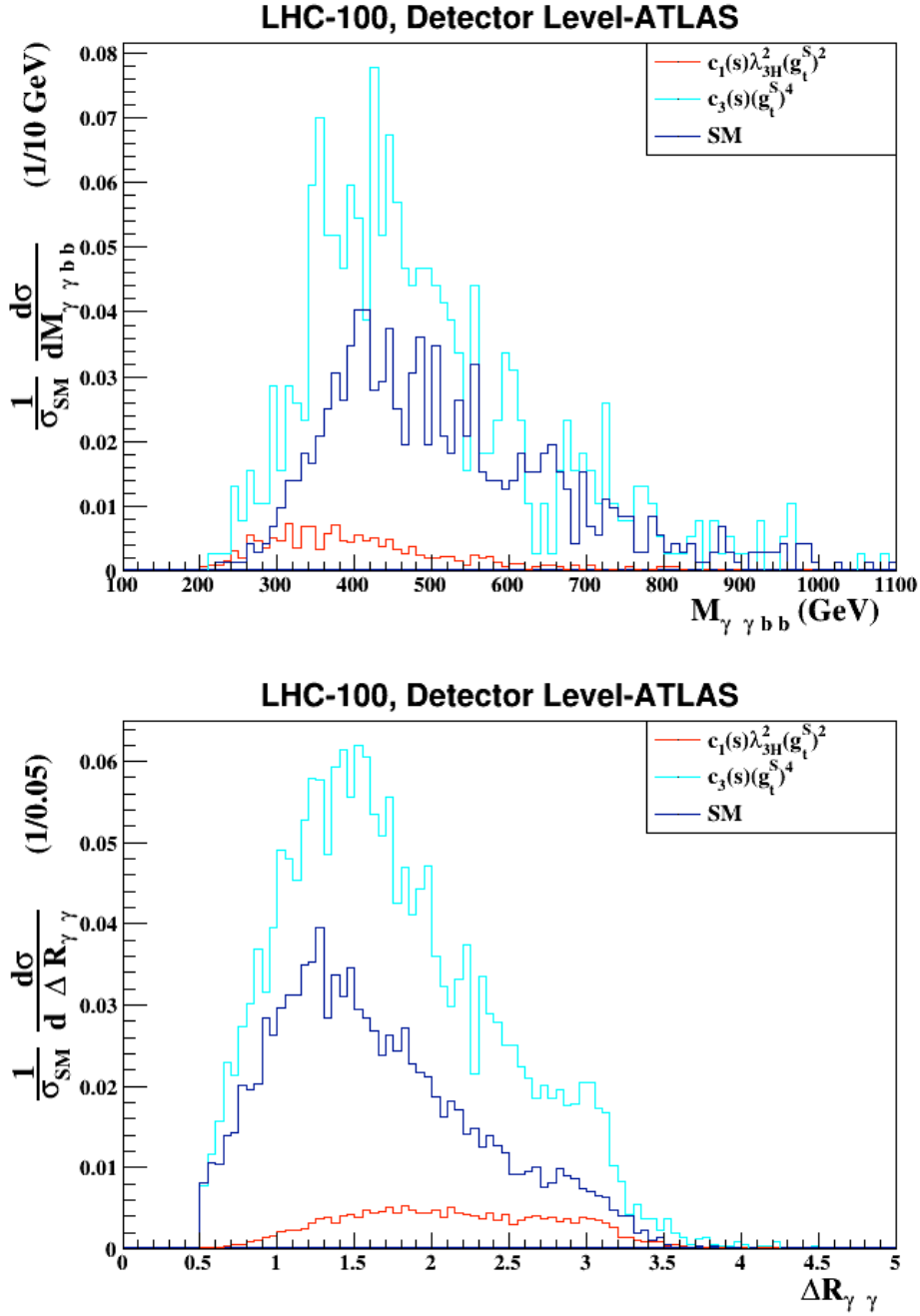


FIG. 20. Distributions in the invariant mass distribution $M_{\gamma\gamma b\bar{b}}$ and the angular separation $\Delta R_{\gamma\gamma}$ in the decay products of the Higgs boson pair with detector simulation at the 100 TeV pp machine.

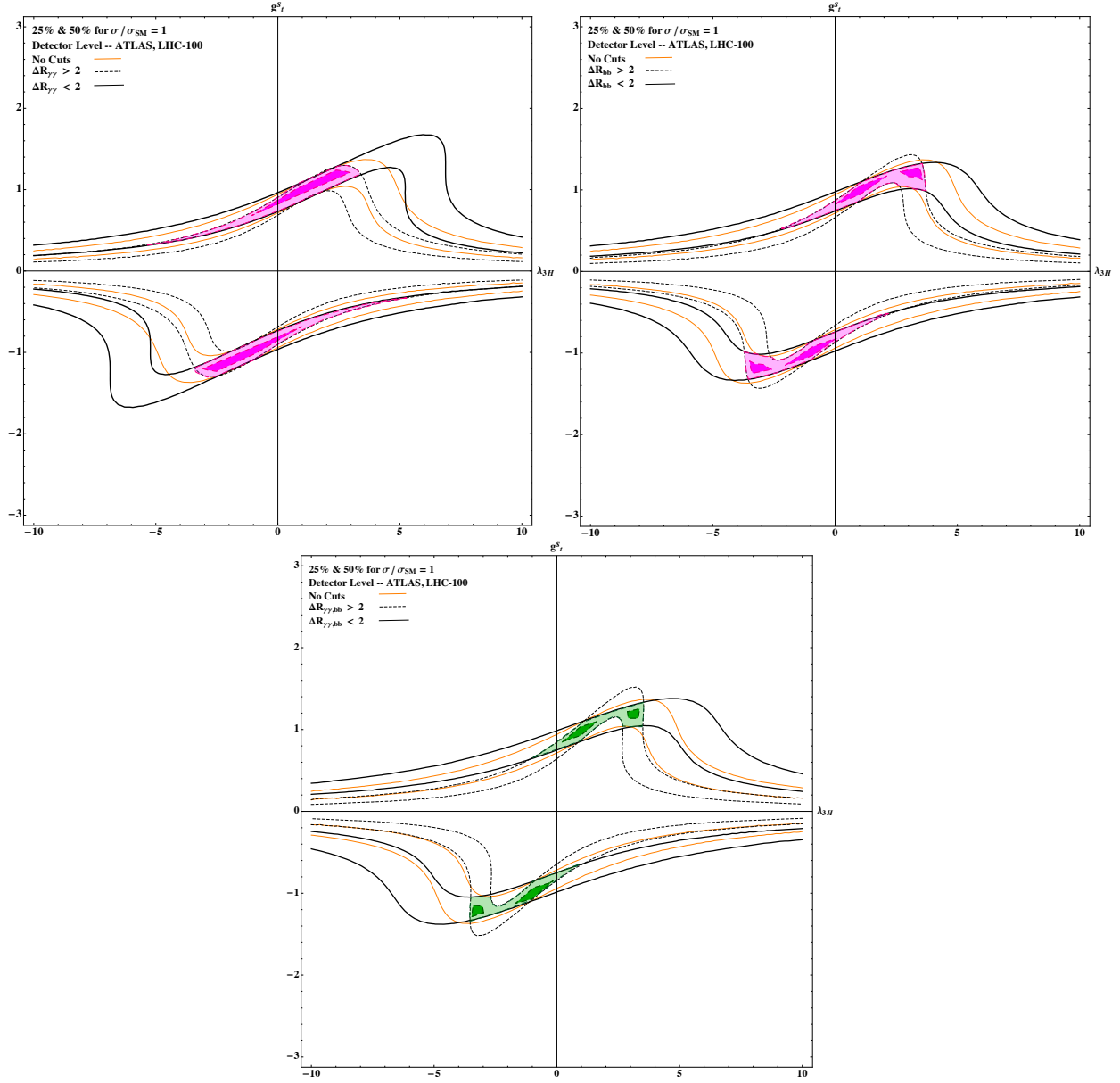


FIG. 21. **CPC1 at 100 TeV:** Exactly the same as Fig. 4, except that it is the case of the 100 TeV pp machine.